PHYSICAL REVIEW D **96,** 026012 (2017)

Inhomogeneous thermal quenches

Kiyoumars A. Sohrabi[*]

Albert Einstein Center for Fundamental Physics, Universität Bern, Sidlerstrasse 5, CH-3012 Bern
and Department of Physics, Brandon University, Brandon, Manitoba R7A 6A9 Canada

(Received 31 March 2016; published 17 July 2017)

We describe holographic thermal quenches that are inhomogeneous in space. The main characteristic of the quench is to take the system far from its equilibrium configuration. Except in special extreme cases, the problem has no analytic solution. Using the numerical holography methods, we study different observables that measure thermalization such as the time evolution of the apparent horizon, two-point Wightman function and entanglement entropy (EE). Having an extra nontrivial spacial direction allows us to study this peculiar generalization since we categorize the problem based on whether we do the measurements along this special direction or perpendicular to it. Exciting new features that are absent in the common computations appear in the literature; the appearance of negative EE valleys surrounding the positive EE hills and abrupt quenches that occupy the whole space at their universal limit are some of the results of this paper. Physical explanation is given, and connections to Cardy's idea of thermalization are discussed.

DOI: 10.1103/PhysRevD.96.026012

I. INTRODUCTION AND MOTIVATION

Experiments of the heavy-ion collisions have provided a magnificent opportunity to study strongly coupled systems [1]. An important part of this study is to understand the physics of the thermalization in which the fascinating state of matter "quark-gluon plasma" has formed [2].

In the last decade, extensive studies of the hot plasmas close to equilibrium using the weakly coupled field theories have been performed. While the regime of the validity of those results is limited, they have contributed a great deal to our physical interpretation [3] and have been the motivation for more complex computational tool boxes.

Gauge/gravity duality [4] together with spectral methods have become a successful phenomenological framework [5,6] to study the above-mentioned systems in the regime where they can be arbitrarily far from equilibrium while the theory is experiencing strongly coupled behaviors. This is indeed the regime in which we are mostly interested to study the physics of thermalization which allows us to gather information about subtle and more realistic setups that were seemingly out of reach. An example of such scenarios often includes the breaking of symmetries to incorporate the realistic features. This can be conformality, supersymmetry or a simple time and spatial translational invariance.

An easy way to construct such a setup that can have the above attributions is deduced by simply making an abrupt change in one or some of the couplings of a microscopic theory, in our context a quantum field theory, that governs the dynamics of the system. Then, the theory is said to undergo a quantum quench [7–9]. The most common type of quench which in part is also very simple to interpret is to change the mass of the Quantum Field Theory (QFT) i.e. to produce a mass gap artificially. As the goal of studying quenches is to observe thermalization, one can see that a rapid change in the mass of the action or the corresponding Hamiltonian will correspond to excess of energy that has to be shared among new degrees of freedom in the new system. The physics of how the quantum system will manage to reach this new state which can or cannot be accompanied by a thermal process will be of great importance to us [7].

Of course, our primary interest is the non-Abelian QCD plasma which has a strongly coupled dynamics. One hopes that QCD's long distance behavior at high temperature can be more or less described by the pure $\mathcal{N} = 4$ super Yang-Mills. In light of this connection, attempts have been made to mimic some aspects of the QCD which maybe enable us to use the AdS/CFT duality. The maximally supersymmetric content of the theory contains degrees of freedom such as adjoint fields that are absent in QCD but still has a good resemblance to the quark-gluon plasma that we are interested in. It turns out that we can modify the $\mathcal{N} = 4$ SYM further to overcome some of the physically unwanted features of the theory. One example, in this regard, is breaking the conformality in $\mathcal{N} = 4$ SYM by adding a bare mass term [10]. The resulting theory is $\mathcal{N} = 2$.[1] with massive hypermultiplets in the adjoint representation i.e. $\mathcal{N} = 2^*$ with a nontrivial RG flow [11]. Note again that at high temperatures this mass deformation will become irrelevant. The superpotential for the hypermultiplet mass term then will consist of structures such as $\mathrm{Tr}Q^2 + \mathrm{Tr}\tilde{Q}^2$

---

[*] SohrabiK@BrandonU.CA

[1] This should not be confused by a closely related model of $\mathcal{N} = 1^*$ $SU(N)$ gauge theory which is another possibility of softly breaking $\mathcal{N} = 4$ by a chiral multiplet mass term.

and $\mathrm{Tr}([Q,\tilde{Q}]\Phi)$ with Q and $\tilde{Q}$ the $\mathcal{N}=2$ hypermultiplets and where Φ is an adjoint chiral superfield which is related to a gauge field under $\mathcal{N}=2$. These superpotential terms have been expanded in terms of their matter content simply in the form [12]

$$\delta S = -2\int d^4x(m_b^2\mathcal{O}_2 + m_f\mathcal{O}_3), \tag{1.1}$$

with operators $\mathcal{O}_2$ and $\mathcal{O}_3$ defined according to

$$\mathcal{O}_2 = \frac{1}{3}\mathrm{Tr}(|\phi_1|^2 + |\phi_2|^2 - 2|\phi_3|^2), \tag{1.2}$$

$$\begin{aligned}\mathcal{O}_3 = &-\mathrm{Tr}(i\psi_1\psi_2 - \sqrt{2}g_{\mathrm{YM}}\phi_3[\phi_1,\phi_1^\dagger] \\ &+ \sqrt{2}g_{\mathrm{YM}}\phi_3[\phi_2^\dagger,\phi_2] + \mathrm{H.c.}) \\ &+ \frac{2}{3}m_f\mathrm{Tr}(|\phi_1|^2 + |\phi_2|^2 + |\phi_3|^2),\end{aligned} \tag{1.3}$$

and m_b and m_f are bosonic and fermionic masses that will be determined below.

The holographic dual (supergravity) of the above theory was studied elegantly by Pilch and Warner in Ref. [11]. In their work, the supergravity scalar fields dual to the operators defined in Eq. (1.2)–Eq. (1.3) named α and χ satisfy a potential and kinetic term given by

$$\mathcal{V} = -\frac{g^2}{4}e^{-4\alpha} - \frac{g^2}{2}e^{2\alpha}\cosh(2\chi) + \frac{g^2}{16}e^{8\alpha}\sinh^2(2\chi), \tag{1.4}$$

$$T = -3(\partial\alpha)^2 - (\partial\chi)^2. \tag{1.5}$$

For more details of the construction and the RG flow, refer to Refs. [13,14]. Having this dictionary for the AdS/CFT duality made exploration of different aspects of the theory that has great resemblance to QCD possible [10]. Particularly, at finite temperatures, thermodynamics of $\mathcal{N}=2^*$ $SU(N)$ gauge theory at large 't Hooft coupling has been at the center of various works. Buchel, Deakin, Kerner, and Liu showed that at temperatures that are near the mass scale of the theory thermodynamics attributed to the mass deformation is irrelevant and derived the finite temperature version of the Pilch-Warner flows at the boundaries [12]. This later study was then extended to find the behavior of the thermal screening masses of the Quark-Gluon Plasma (QGP) and beyond to lower temperatures [15]. Various aspects of the free energy of the $\mathcal{N}=2^*$ were reported in Ref. [16], and further on, corrections to the transport coefficients were derived [17]. For a work on finite baryon density in this context, refer to Ref. [18].

An enlightening simplicity appears in the regime where $m_{b,f}/T \ll 1$ since in this limit a black hole has formed inside and the boundary of the bulk space will be asymptotically an anti-de Sitter (AdS) space. This motivates us [19] to expand the scalar fields in Eq. (1.4) to obtain

$$\begin{aligned}S_5 = \frac{1}{16\pi G_5}\int d^5x\sqrt{-g}\Big(&R + 12 - \frac{1}{2}(\partial\phi)^2 \\ &- \frac{1}{2}m^2\phi^2 + \mathcal{O}(\phi^3)\Big),\end{aligned} \tag{1.6}$$

where in the above $\phi \in \{2\sqrt{6}\alpha, 2\sqrt{2}\chi\}$ with the corresponding masses $m^2 \in \{-4,-3\}$ and $G_5 \equiv \frac{\pi}{2N_c^2}$. Note that we have put the radius of AdS in Eq. (1.6) equal to 1. It must be clear that in the above range of temperatures, we are looking at large scale black holes and it is reasonable to treat the amplitudes of the scalar fields perturbatively with respect to the former length scales and the length $l \sim m_f/T$ will be used to truncate the backreaction.

Now, we are in the position to make the connection to the quench picture more concrete. As mentioned above, the result of the mass deformation is to map our starting point i.e. S_{SYM} of $\mathcal{N}=4$ into $S_{\mathrm{SYM}} + \delta S$ with δS defined already in Eq. (1.1). The operators $\mathcal{O}_2$ and $\mathcal{O}_3$ that are dual to the scalar field ϕ, with different masses, have different dimensions based on their structures in the superpotential. If Δ is the dimension of each operator, then the corresponding mass of the dual scalar field will satisfy [15] $\Delta(\Delta-4) = m^2$. In other words, in the boundary theory, one of the operators, namely $\mathcal{O}_3$, couples to a fermionic mass m_f, and $\mathcal{O}_2$ couples to a bosonic mass. Similar to Ref. [20], we will concentrate only on the fermionic operator in this paper and fix the dual mass of the scalar field to $m^2 = -3$.

By fixing the parameters of the bulk theory, it was remarkably suggested [19] to use a toy profile for m_f. Among various choices, the profile that produces a mass gap is particularly interesting. This evolution can be simply written in terms of the step function, $m_f = m_0\theta(\tau)$, as a function of real time or a more smooth and articulated variation of it,

$$m_f = \frac{1}{2}m_0[1 \pm \tanh(\tau)]. \tag{1.7}$$

Either way, the system can start from a massless (massive) ground state and end up in a massive (massless) eventual state after thermalization [20]. We refer to this setup as the *homogeneous* scenario. Calabrese and Cardy came up with an attractive idea to describe the effect of such an evolution of a mass gap [7]. In their "horizon effect" picture, semiclassical propagations (quasiparticles)[2] at the initial state, or in fact every imaginary Cauchy surface that was satisfying causality, were responsible for the later thermalization of the system. A key point that came up in

---

[2] The concept of quasiparticles has an old history in thermal QFT, and it has been used successfully in the perturbative and close to equilibrium physics, but not at far from equilibrium and strongly coupled systems.

their discussion was to associate with each coherent set of particles an effective temperature $T_{\rm eff}$. Then, at later times, interference of incoherent quasiparticles that sets off their journey in an uncorrelated fashion derives the system to thermalization. It was further speculated by the authors that this can be a thermal process such as a thermal diffusion. To clarify this idea further, in Ref. [8], they studied the evolution of the mass deformation with an inhomogeneous initial state in models such as conformal and free field theory.

These ideas are worth a second look. We are curious to know if the final stationary state of matter depends in any way on the initial state to begin with. Having an extra toy dimension that affects the dynamics will help us in this direction. If the theory is very symmetric, motion of trajectories will be confined to a specific section of the phase space; this should be compared with a less symmetric case in which trajectories will occupy the whole space of solutions and therefore a more realistic situation to study in the case of the thermalization. Reference [21] has looked into this point with different settings.

We will not consider an inhomogeneous initial state but rather extend Eq. (1.7) to include the following form:

$$m_f = \frac{1}{2}\left[1+\tanh\left(\frac{\tau}{\alpha}\right)\right]e^{-\frac{x^2}{\sigma^2}}. \tag{1.8}$$

This is the *inhomogeneous* scenario that we will consider. The response of the strongly coupled $\mathcal{N}=4$ supersymmetric Yang-Mills thermal plasma will be studied while it is quenched by tuning parameters α and σ that play the role of different scales for perturbations in time and space respectively. Note that the natural scale of the problem is set by the initial scale of the horizon, πT.[3]

We will consider a cherry picked range of α and σ. In this way, we can have more control and better insight into the physics of thermalization. The chosen values for the parameters in Eq. (1.8) in the text correspond to interesting physics such as the limit of slow/fast quenches with various sizes of spacial inhomogeneity.

To solve the problem, we will be using an ansatz with four arbitrary[4] functions of space and time with x being the coordinate in which profiles are inhomogeneous with respect to it,

$$\begin{aligned} ds_5^2 = &-A(\tau,\rho,x)d\tau^2 + \Sigma_d(\tau,\rho,x)^2dx^2 + \Sigma_b(\tau,\rho,x)^2d\vec{y}^2 \\ &+ 2\Xi(\tau,\rho,x)d\tau dx - 2\frac{d\rho d\tau}{\rho^2}, \end{aligned} \tag{1.9}$$

and if for the brevity of argument, we neglect the logarithmic corrections and higher-order terms here, the boundary could be written as[5]

$$\phi = l(\rho p_0 + \rho^2\partial_\tau p_0 + \rho^3 p_2) + \mathcal{O}(l^3,\rho^4), \tag{1.10}$$

$$A = \frac{1}{\rho^2} - \rho^2 + l^2\left(-\frac{1}{6}p_0^2 + \rho^2 a_2\right) + \mathcal{O}(l^4,\rho^2\ln\rho), \tag{1.11}$$

$$\Sigma_d = \frac{1}{\rho} + l^2\left(-\rho^2\frac{p_0^2}{12} - \rho^3\frac{p_0\partial_\tau p_0}{9} + \rho^4 d_4\right) + \mathcal{O}(l^4,\rho^4\ln\rho), \tag{1.12}$$

$$\Sigma_b = \frac{1}{\rho} + l^2\left(-\rho^2\frac{p_0^2}{12} - \rho^3\frac{p_0\partial_\tau p_0}{9} + \rho^4 b_4\right) + \mathcal{O}(l^4,\rho^4\ln\rho), \tag{1.13}$$

$$\Xi = l^2\left(-\rho\frac{p_0\partial_x p_0}{9} + \rho^2 f_2\right) + \mathcal{O}(l^3,\rho^2\ln\rho), \tag{1.14}$$

where in the above p_0, p_2, a_2, b_4, d_4 and f_2 depend on (τ, x). Note that from the AdS/CFT dictionary $m_f = p_0$. These functions will satisfy Einstein equations that are coupled second-order partial differential equations. To solve them numerically, we will apply spectral methods and techniques developed by Chesler and Yaffe [5] and use the Dirichlet boundary condition for the longitudinal direction. The accuracy of our physical results is certainly limited to our computational resources. While we could quantify the effect of the numerical artifacts to be of a few percent, to our knowledge, none of physical conclusions that are deduced is affected by them.

In this paper, we study various observables already in the literature such as the apparent horizon, two-point Wightman functions and entanglement entropy (EE). Our goal is to study the thermalization under the quench in Eq. (1.8) for various parameters with a special emphasis on the study of EE. In Sec. II, we look into these different nonlocal observables as a measure of the thermalization, and different aspects of them will be studied in detail. In Sec. III, we recap the conclusions and the physical picture deduced from the simulations in previous sections. Section IV is dedicated to a discussion on fast quenches, and the Appendix gives a thorough derivation of the equations of motion and numerics.

II. THERMALIZATION OBSERVABLES

A. Apparent horizon

One of the most important quantities in the description of the thermodynamics of a black hole is its statistical entropy as a measure of the number of quantum states.

---

[3] For numerical purposes, we factor out scales of the coordinates such as $\rho_{\rm new} = \frac{\pi T}{r_{\rm old}}$, $x_{\rm new} = \frac{x_{\rm old}}{\pi T}$ and $\tau_{\rm new} = \pi T \tau_{\rm old}$. And we will be working with the "new" variables. This factorization also affects components of the metric for instance $A_{\rm new} = (\pi T)^2 A_{\rm old}, \ldots$

[4] Please refer to [22].

[5] The complete list is outlined in the appendix.

Hawking's famous area relation, $S = \frac{A_h}{4G_5}$, makes a connection between this entropy and the area of the black hole's horizon. The radius of the former area is determined by the position of the horizon, and in our scenario as the scalar field falls into the black hole and radiates, the black hole expands, and its rate is directly related to the behavior of the radius.

We consider the metric in Eq. (1.9) with a simplifying feature of setting a cutoff in the backreaction at second order, explicitly assuming[6]

$$A(\tau,\rho,x) = \frac{1}{\rho^2} - \rho^2 + l^2\hat{A}(\tau,\rho,x) + \mathcal{O}(l^4), \tag{2.1}$$

$$\Sigma(\tau,\rho,x) = \frac{1}{\rho} e^{l^2\hat{\Sigma}(\tau,\rho,x)} + \mathcal{O}(l^4), \tag{2.2}$$

$$\Xi(\tau,\rho,x) = l^2\hat{\Xi} + \mathcal{O}(l^3), \tag{2.3}$$

where Σ in the above notation can be either of Σ_b and Σ_d and the expansion parameter is determined by $l \sim m_f/T$. Basically, the argument is that we look at the variations of ϕ at the order of l and neglect the backreaction on itself. Implementing this assumption in the Einstein equations allows us to truncate the series at $\mathcal{O}(l^3)$ or $\mathcal{O}(l^4)$ on different metric components. For an interesting discussion of the thermodynamics of the model, refer to Ref. [23]. In the following, we use the above components to study the behavior of the apparent horizon of the black hole deep in the bulk.

In a much simpler case where $\Sigma_d = \Sigma_b \equiv \Sigma$ (the homogeneous spacetime), the equation for the position of the trapping surface follows from $d_+\Sigma = 0$ with $d_+ \equiv \partial_\tau - \frac{A\rho^2}{2}\partial_\rho$. In the general case [22], this equation is modified to[7]

$$d_+\Sigma = -\frac{1}{2}\partial_\rho\Sigma\Xi^2 + \frac{1}{3}\Sigma\nabla\cdot\Xi \tag{2.4}$$

with Σ now given by $\Sigma \equiv (\Sigma_d\Sigma_b^2)^{1/3}$. Applying the expansions in Eq. (2.1)–Eq. (2.3) gives the position of the trapping surface

$$\rho_h(\tau,x) = \left[\frac{\hat{A}(\tau,\rho,x)}{4} + \frac{\partial_\tau\hat{\Sigma}_d(\tau,\rho,x)}{6} + \frac{\partial_\tau\hat{\Sigma}_b(\tau,\rho,x)}{3} - \frac{\partial_x\hat{\Xi}(\tau,\rho,x)}{6}\right]_{\rho=1}. \tag{2.5}$$

Knowing the position of the apparent horizon, ρ_h, the natural quantity to calculate is the volume of the horizon. The volume density of the entropy given by $\mathcal{S} = \frac{V_h}{4G_5}$ corresponds to the explicit expression for the perturbation of the volume element

$$V_h = \Sigma_d\Sigma_b^2 \equiv 1 + l^2\delta V_h, \tag{2.6}$$

where it has to be calculated at $(\tau, 1 + l^2\rho_h, x)$. This gives the final expression for variation in the volume element of the apparent horizon,

$$\delta V_h = \left[-\frac{3}{4}\hat{A} - \frac{\partial_\tau\hat{\Sigma}_d}{2} + \frac{\partial_x\hat{\Xi}}{2} - \partial_\tau\hat{\Sigma}_b + \hat{\Sigma}_d + 2\hat{\Sigma}_b\right]_{\rho=1}. \tag{2.7}$$

From the above expression, we can see that the introduction of the inhomogeneity directly changes the location of the apparent horizon in comparison with the previous calculations in Refs. [20,24].

As a reference, Fig. 1(a) shows the plot for $p_0(\tau,x)$, read it m_f, as a function of real time τ and inhomogeneous direction x. This is equivalent to the profile of the scalar field that is falling into the black hole from the boundary and the effect of this infall can be seen in the fluctuations of the apparent horizon in Figs. 1(b)–1(f) in $x-\tau$ coordinates. These plots that match those of Ref. [20] have been specifically chosen as they show different physics as we vary the tuning parameters. One first clear point is that they all roughly imitate behaviors of their sources. Choosing $x = 0$ in $p_0(\tau,x)$ will reduce our problem to Ref. [20]. As it is clear from Figs. 1(b)–v, their behaviors along $x = 0$ are very similar. They all follow the profile of $p_0(\tau, x = 0)$. But they follow different patterns along the inhomogeneous direction. In $p_0(\tau,x)$, there are Gaussian profiles in the x direction with amplitudes that are almost constant far away from $\tau = 0$, either $\tau > 0$ or $\tau < 0$. Close to $\tau = 0$, the amplitude of the Gaussian distribution increases linearly. This is when the quench has been turned on and in the vacuum of the QFT a mass gap has been formed. This is evident in Figs. 1(b), 1(c) and 1(f) for $\tau = 0$. It is an interesting fact that at this moment excitations occupy a length equal to the width of the initial Gaussian profile and their amplitudes seem to follow a universal behavior, occupying the whole available space.

As we reduce the value of α in $p_0(\tau,x)$, excitations will not only occupy the available space at the $\tau = 0$ but also overrun the original profile of $p_0(\tau,x)$ for all $\tau > 0$ as seen in Figs. 1(b)–1(e). In fact, it is very hard to distinguish between Figs. 1(d) and 1(e), although they physically belong to different sizes of the mass gaps. This is the universal behavior associated with the abrupt quenches that have been discovered in Refs. [25,26].

---

[6] Since the metric is invariant under the residual diffeomorphism $r \to r + f(\tau)$ with $r \equiv 1/\rho$, we use this property to fix the expansion of $A(\tau,\rho,x)$ not to have any linear term in r.

[7] The ∇ and the dot product are defined according to $\hat{g}$ with spatial components given by $\hat{g}_{11} = (\frac{\Sigma_d}{\Sigma_b})^{4/3}$ and $\hat{g}_{22} = \hat{g}_{33} = (\frac{\Sigma_b}{\Sigma_d})^{2/3}$.

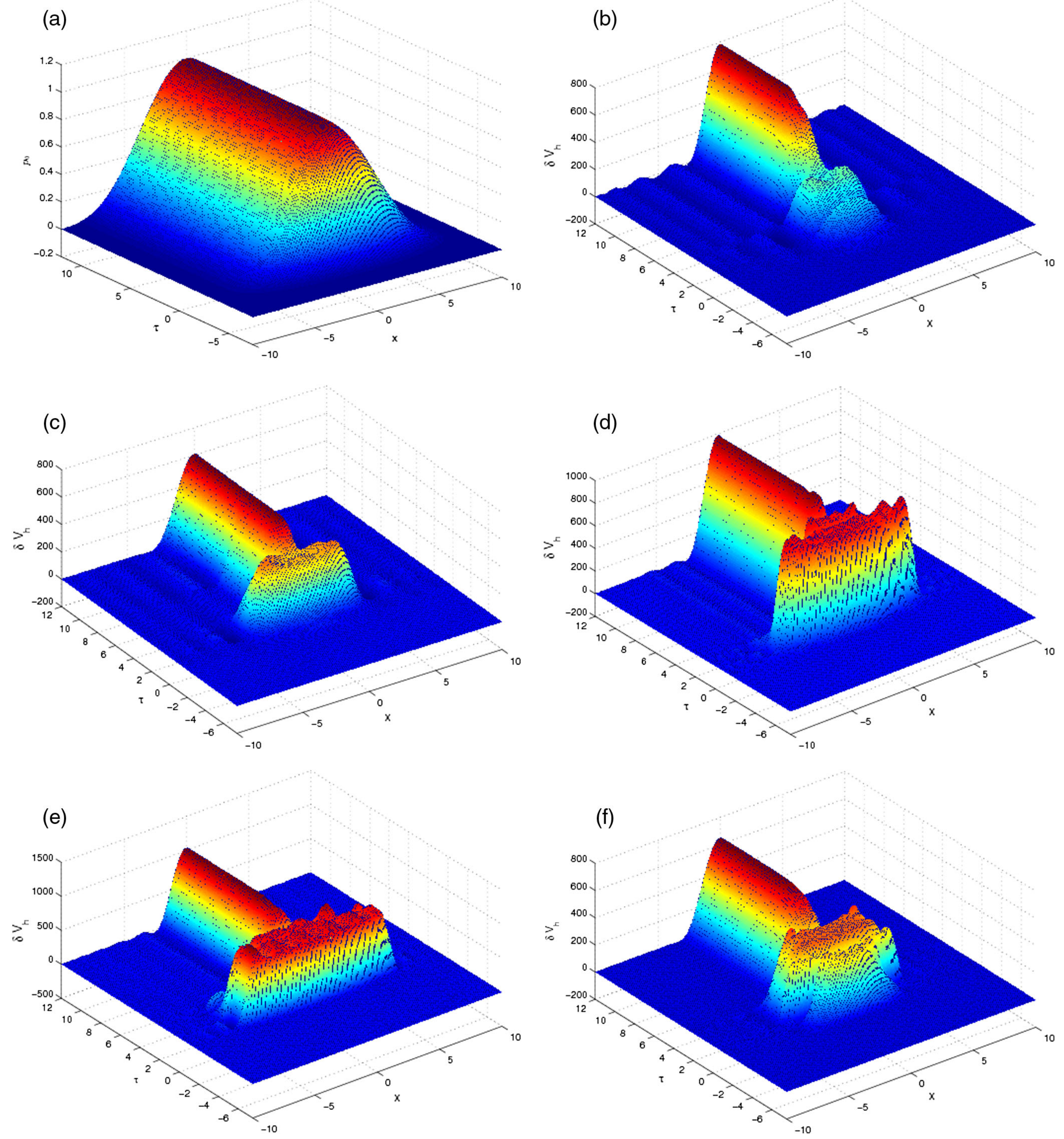

FIG. 1. Figure (a) is the profile of p_0 that is being sent into the black hole. The rest of the plots are time evolutions of variations in the radial position of the horizon. In (b), (c), (d) and (e), plots are drawn for a fixed value of $\sigma = \sqrt{L_x}$ with $L_x = 10$ the length of the domain in the x direction. The varying parameters are correspondingly $\alpha \in \{1, \frac{1}{2}, \frac{1}{4}, \frac{1}{8}\}$. In (f), these parameters are $\alpha = 1$ and $\sigma = \sqrt{1.5L_x}$. The interpolations are based on $N_x = N_\rho = 20$–30, the number of Chebyshev points along the inhomogeneous direction x and radial direction ρ. The number of time steps used for the fourth-order Runge-Kutta varies between 7810 and 17,560.

An interesting feature is captured in Fig. 1(f). By increasing σ, the tuning parameter corresponding to the width of the Gaussian distribution, mass gap excitations will fill up the available space.

Some of the features in the plots below should not be confused by physics. They are discretization artifacts, and one can in principle factor them out by improving the computational resources. For instance, the amplitude of

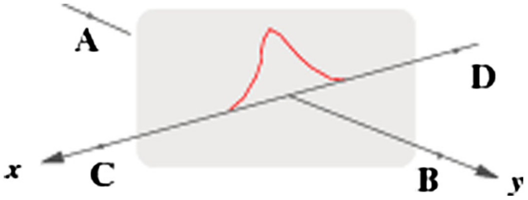

FIG. 2. The disturbance drawn in red pen is that of a Gaussian function, representing the inhomogeneity. We are interested in the correlation of points off this plane, i.e. points A and B in case I. Similarly, in case II, the correlation between C and D will be studied. Note the resemblance of the setup to the elliptic flow in heavy-ion collisions.

the corrugations in the flat areas surrounding the bump to the highest peak is at maximum 5%. Similarly, the local peaks on top of the bumps at the time of switching the quench are at maximum 9%. A short discussion about the size of the numerical artifacts and their effects on the thermalization is given in Secs. A 1 and A 2.

B. Two-point correlator

Two-point Wightman functions are good candidates of probing thermalization. For operators with large masses, the correlation functions will have a simple interpretation in term of spacelike geodesics that connect two sample points on the boundary of the conformal field theory (CFT) through the bulk space. Since we have a special direction which is the direction of the inhomogeneity, we can categorize our setup into two groups. Case I will be the situation where this special direction is orthogonal to the axis of observation, and case II refers to the situation where the points chosen are along the axis of the inhomogeneity. This is explained in Fig. 2.

Similar categorization also applies to our discussion in the next section where we extend this setup and study thermalization of the quenches by the entanglement entropy.

1. Case I: Plane A–B

To see the effect of the quenches, we are interested in the length of a geodesic that stretches along one of the spatial directions. The other simplifying assumption here is that, similar to Ref. [20], we look into the correlator of operators with large conformal dimensions.[8] Then, the two-point Wightman function will be proportional to the length of the boundary-to-boundary spacelike geodesic [27].

For simplicity, our choice is the curve that satisfies boundary conditions, $\tau_1 = \tau_*$, $y_1 = -y_m$, $x_1 = z_1 = 0$ and $\tau_2 = \tau_*$, $y_2 = y_m$, $x_2 = z_2 = 0$, in other words, not the specific direction that the inhomogeneity will act on. In this setup, the geodesic connects points A and B through their extension in the bulk. The inhomogeneity appears at $\mathcal{O}(l^2)$ along the axis where points C and D are positioned. To see how the quench affects the geodesic as we mentioned before, we choose a cutoff for the backreaction at $\mathcal{O}(l^2)$. The effect of this backreaction on the coordinates will be parametrized by

$$\tau = \tau_0 + l^2\tau_2, \qquad \rho = \rho_0 + l^2\rho_2, \qquad x = l^2 x_2. \tag{2.8}$$

Our former boundary condition imposes $\tau_0 = \tau_*$. It is instructive to compute the geodesic first, to see explicitly the effect of the inhomogeneity. Since the geodesic equations follow from $\frac{d^2x^\kappa}{d\lambda^2} + \Gamma^\kappa_{\mu\nu}\frac{dx^\mu}{d\lambda}\frac{dx^\nu}{d\lambda} = 0$ in some general affine parametrization λ in cases I and II, different equations of motion will be derived. It is also interesting to see how the inhomogeneity affects the geodesic beyond our approximation for the backreaction. The equations of motion in this case are cumbersome, and it suffices to mention that the above parametrization will still work out to solve the equations of motion.

Geodesic equation for $\boldsymbol{\tau}$.—At the zeroth order, the equation is trivially satisfied; when $l = 0$, one can see that

$$\ddot{\tau}_0 - \frac{1}{\rho_0}[1 - (\dot{\tau}_0)^2(1 + \rho_0^4)] = 0, \tag{2.9}$$

and at the second order, we get

$$\ddot{\tau}_2 + 2\frac{\dot{\tau}_0\dot{\tau}_2}{\rho_0}(1 + \rho_0^4) + \frac{\rho_2}{\rho_0^2}[\dot{y}_0^2 - \dot{\tau}_0^2(1 - 3\rho_0^4)] - \frac{2\dot{y}_0^2\hat{\Sigma}_b}{\rho_0} \\ - \frac{1}{2}\dot{\tau}_0^2\rho_0^2\partial_\rho\hat{A} + \partial_\rho\hat{\Sigma}_b = 0, \tag{2.10}$$

where in the above we have constrained the geodesic by $\dot{x}_0 = \dot{z}_0 = 0$. Also note that the metric components depend on $(\tau_0, \rho_0, x_0, y_0)$ with $\tau_0(y_0)$ and $\rho_0(y_0)$. This means that we are looking at constant intervals on the geodesic along the x axis.

Geodesic equation for $\boldsymbol{\rho}$.—At zeroth order, the geodesic equation for $\boldsymbol{\rho}$ reads

$$\ddot{\rho}_0 + \frac{1}{\rho_0}[\dot{y}_0^2 - \dot{\tau}_0^2 - 2\dot{\tau}_0\dot{\rho}_0 - 2\dot{\rho}_0^2] \\ - \rho_0^3(\dot{y}_0^2 + 2\dot{\tau}_0\dot{\rho}_0 - \rho_0^4\dot{\tau}_0^2) = 0, \tag{2.11}$$

and for $\mathcal{O}(l^2)$,

---

[8] This limit omits the possibility of studying the correlator of the quenching operator itself.

$$\ddot{\rho}_2 + \dot{\rho}_2\left(-2\frac{\dot{\tau}_0}{\rho_0} - 4\frac{\dot{\rho}_0}{\rho_0} - 2\dot{\tau}_0\rho_0^3\right) + \dot{\tau}_2\left(-2\frac{\dot{\tau}_0}{\rho_0} - 2\frac{\dot{\rho}_0}{\rho_0} - 2\dot{\rho}_0\rho_0^3 + 2\dot{\tau}_0\rho_0^7\right)$$
$$+ \rho_2\left(-\frac{\dot{y}_0^2}{\rho_0^2} + \frac{\dot{\tau}_0^2}{\rho_0^2} + 2\frac{\dot{\tau}_0\dot{\rho}_0}{\rho_0^2} + 2\frac{\dot{\rho}_0^2}{\rho_0^2} - 3\dot{y}_0^2\rho_0^2 - 6\dot{\tau}_0\dot{\rho}_0\rho_0^2 + 7\dot{\tau}_0^2\rho_0^6\right) + \hat{A}(\dot{y}_0^2\rho_0 - \dot{\tau}_0^2\rho_0 - \dot{\tau}_0^2\rho_0^5)$$
$$+ \frac{\partial_\rho\hat{A}}{2\rho_0^2}(\dot{\tau}_0^2\rho_0^2 + 2\dot{\tau}_0\dot{\rho}_0\rho_0^2 - \dot{\tau}_0^2\rho_0^6) + \frac{2\dot{y}_0^2\hat{\Sigma}_b}{\rho_0}(1 - \rho_0^4) + \dot{y}_0^2\partial_\rho\hat{\Sigma}_b(-1 + \rho_0^4) + \frac{1}{2}\dot{\tau}_0^2\rho_0^2\partial_\tau\hat{A} + \dot{y}_0^2\partial_\tau\hat{\Sigma}_b = 0. \quad (2.12)$$

Inhomogeneous direction $\boldsymbol{x}_2$.—Simplifying the equation will yield

$$\ddot{x}_2 - 2\frac{\dot{\rho}_0\dot{x}_2}{\rho_0} + \rho_0\Xi[\dot{y}_0^2 - (\dot{\tau}_0)^2(1 + \rho_0^4)] + \frac{1}{2}\dot{\tau}_0^2\rho_0^2\partial_x\hat{A}$$
$$- \dot{y}_0^2\partial_x\hat{\Sigma}_b + \rho_0^2\dot{\tau}_0(\dot{\rho}_0\partial_\rho\hat{\Xi}_f + \dot{\tau}_0\partial_\tau\hat{\Xi}_f) = 0. \quad (2.13)$$

As we said before, we are looking at constant intervals along the x axis and by varying the affine parameter that causes the geodesic to go deeper in the bulk; a nonzero value for x_2 will be produced. Note the ∂_x in Eq. (2.13), which produce a distance of the order of l^2 between constant intervals.

From the metric compatibility condition, $\epsilon = -g_{\mu\nu}\frac{dx^\mu}{d\lambda}\frac{dx^\nu}{d\lambda}$, and the condition on spacelike geodesics, $\epsilon = -1$, at zeroth order in l, one obtains

$$-\eta_{\mu\nu}\dot{x}_0^\mu\dot{x}_0^\nu + 2\dot{\tau}_0\dot{\rho}_0 - \dot{\tau}_0^2\rho_0^4 = -\rho_0^2, \quad (2.14)$$

in which we have to impose $\dot{x}_0 = \dot{z}_0 = 0$ and $\dot{y}_0 = 1$. After expanding to $\mathcal{O}(l^2)$, the corresponding equation simplifies to

$$\frac{1}{\rho_0^2}(\dot{\tau}_0\dot{\tau}_2 + \dot{\tau}_2\dot{\rho}_0 + \dot{\tau}_0\dot{\rho}_2 - \dot{y}_0^2\hat{\Sigma}_b) - \dot{\tau}_0\dot{\tau}_2\rho_0^2$$
$$+ \frac{\rho_2}{\rho_0^3}(\dot{y}_0^2 - \dot{\tau}_0^2 - 2\dot{\tau}_0\dot{\rho}_0) - \dot{\tau}_0^2\rho_0\rho_2 + \frac{1}{2}\dot{\tau}_0^2\hat{A} = 0. \quad (2.15)$$

Similar expansion to the order of $\mathcal{O}(l^2)$ for the geodesic equations in the direction of y and z will produce

$$-\frac{\dot{\rho}_2}{\rho_0} + \frac{\rho_2}{\rho_0^2}\dot{\rho}_0 + \dot{\rho}_0\partial_\rho\Sigma_b + \dot{\tau}_0\partial_\tau\Sigma_b = 0. \quad (2.16)$$

The Killing vector in the y direction satisfies $\Sigma_b^2\dot{y}_0 = \text{const}$, expanding to zeroth order will yield $\dot{y}_0 = \rho_0^2 \times \text{conts}$, and this will fix the value of $\dot{y}_0$ in Eq. (2.9)–Eq. (2.15).

After this short study of the behavior of the geodesics under the quench, we can compute the length of geodesics of interest. The length of the geodesic connecting operators inserted at $(\tau_1 = \tau_*, y_1 = -y_m, x_1 = z_1 = 0)$ and $(\tau_2 = \tau_*, y_2 = y_m, x_2 = z_2 = 0)$ evaluates to

$$\mathcal{L} = \int_{-y_m}^{y_m} dy_0\sqrt{\Sigma_b^2 + \Sigma_d\dot{x}^2 - A\dot{\tau}^2 + 2\Xi\dot{x}\,\dot{\tau} - 2\frac{\dot{\rho}\,\dot{\tau}}{\rho^2}}, \quad (2.17)$$

with all the metric components as a function of (τ, ρ, x, y). After expanding to the first order of l^2, we get a correction for the length of the geodesic that has the form of $\mathcal{L} = \mathcal{L}_0 + l^2\mathcal{L}_2$, with

$$\mathcal{L}_0 = \int_{-y_m}^{y_m} dy_0\frac{\sqrt{D(\tau_0, \rho_0, x_*)}}{\rho_0}; \quad (2.18)$$

here, x_* is the boundary coordinate in the inhomogeneous direction. The second-order correction is given by

$$\mathcal{L}_2 = \int_{-y_m}^{y_m} dy_0\left[\frac{\hat{\Sigma}_b - \dot{\tau}_0^2\rho_0^2\hat{A}/2}{\rho_0\sqrt{D}} - \frac{\dot{\rho}_0 + \dot{\tau}_0(1 - \rho_0^4)}{\rho_0\sqrt{D}}\dot{\tau}_2\right.$$
$$\left. - \frac{D - 2\dot{\tau}_0\rho_0^4}{\rho_0^2\sqrt{D}}\rho_2 - \frac{\dot{\tau}_0}{\rho_0\sqrt{D}}\dot{\rho}_2\right], \quad (2.19)$$

with

$$D = 1 - 2\dot{\tau}_0\dot{\rho}_0 + \dot{\tau}_0^2(-1 + \rho_0^4). \quad (2.20)$$

Note that if we were assuming $\dot{x}_0 \neq 0$ then there would be a term proportional to x_2 in Eq. (2.19). It is convenient to use the equations of motion for the geodesics for the last three terms in Eq. (2.19) to show that the total contribution is zero after a partial integration. This is a consequence of perturbation around the extremal trajectory as it was noticed in Ref. [20].

The constraint on the static geodesics comes from $K_\mu\frac{dx^\mu}{d\lambda} = \text{const}$. In the absence of the quench, time is a Killing vector. With $K_\tau = g_{\tau\tau}$, $K_\rho = g_{\rho\tau}$ and $K_x = g_{x\tau}$, the zeroth-order equation is given by

$$(\rho_0^4 - 1)\dot{\tau}_0 - \dot{\rho}_0 = \text{const} \quad (2.21)$$

Another way of seeing this is from the zeroth-order geodesic equation for y. At the horizon $\rho_0 = 1$ and $\dot{\rho}_0 = 0$, this fixes the constant coefficient to zero. The general solution is [20]

$$\frac{d\tau_0}{d\rho_0} = -\frac{1}{1 - \rho_0^4}, \quad \text{or}$$
$$\tau_0(\rho_0) = \tau_* - \tan^{-1}(\rho_0) - \tanh^{-1}(\rho_0); \quad (2.22)$$

here, τ_* is the time on the boundary as an observer in the bulk reaches the boundary at $\rho \to 0$. From the compatibility condition of the metric, Eq. (2.14), we have

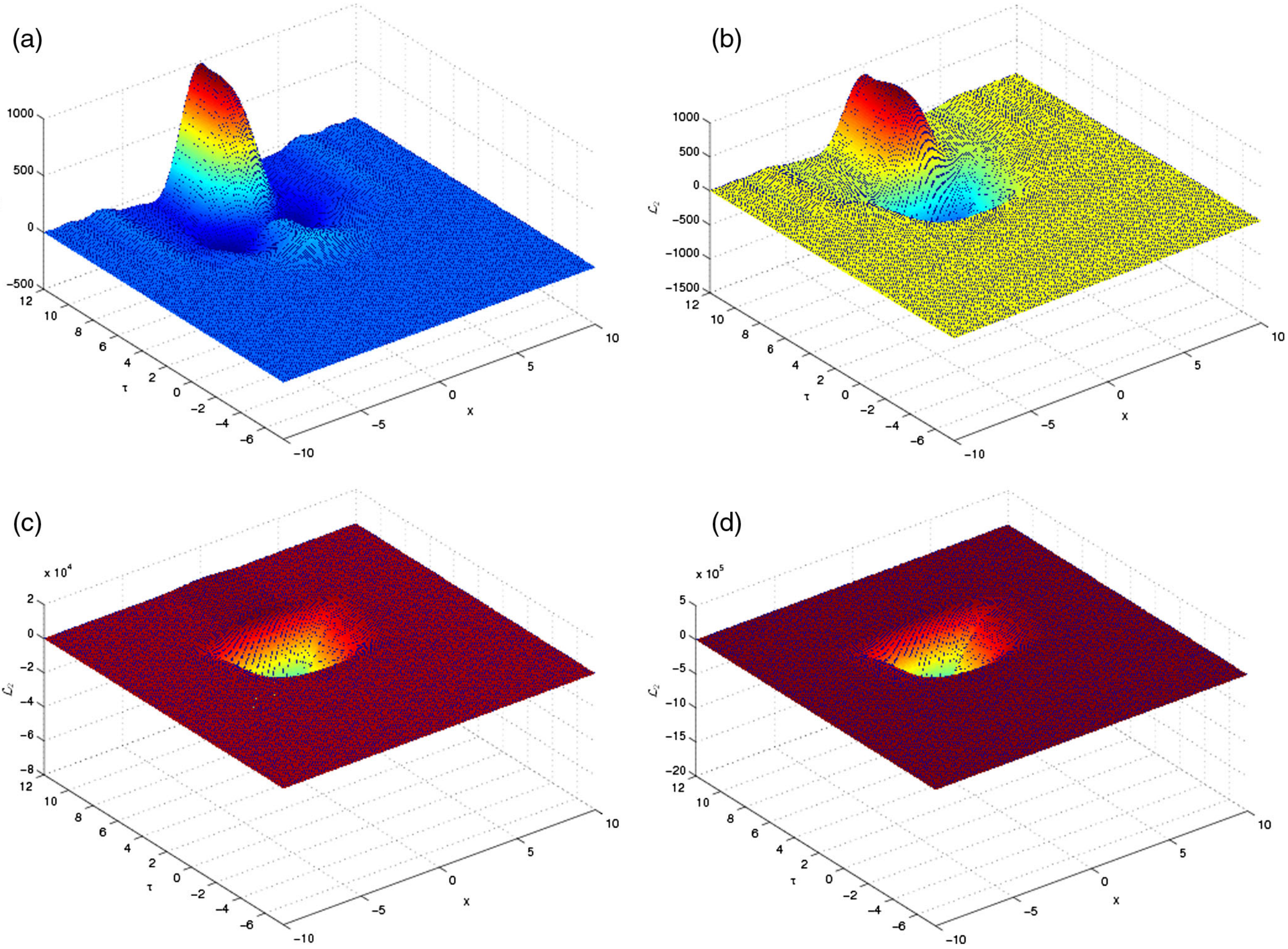

FIG. 3. Time evolution of the two-point Wightman functions for operators with large conformal dimensions. Figures in (a), (b), (c) and (d) are plotted for $\alpha \in \{1, \frac{1}{2}, \frac{1}{4}, \frac{1}{8}\}$ and $\sigma = \sqrt{L_x}$. The interpolation of points are based on $N_x = N_\rho = 20{-}30$ along the inhomogeneity direction x and radial direction ρ. The number of time steps for 4 step Runge–Kutta methods (RK4) is $7810 - 17,560$.

$$[1 + (\rho_0^4 - 1)\dot{\tau}_0^2 - 2\dot{\tau}_0\dot{\rho}_0]\rho_0^2 = \rho_m^2, \tag{2.23}$$

where the constant ρ_m is the maximum value for the radius of the arc that attaches the two points on the boundary. Thus, Eq. (2.19) reduces to

$$\mathcal{L}_2 = -\frac{2}{\rho_m}\int_0^{\rho_m} d\rho_0 \frac{\hat{\Sigma}_b - \dot{\tau}_0^2\rho_0^2\hat{A}/2}{\dot{\rho}_0}, \tag{2.24}$$

where, in the above, the metric components of $\hat{\Sigma}_b$, $\hat{\Sigma}_d$ and $\hat{A}$ depend on (τ_0, ρ_0, x_*) with $\tau_0(y_0)$ and $\rho_0(y_0)$. This is exactly the result in Ref. [20] with the exception that now the profile of the geodesic is nonlinearly a function of the x_*. To prepare the integral for numerics following Ref. [20], after a change of variable such as $\rho_0 = \rho_m(1 - q^2)$, the former expression takes the following form,

$$\mathcal{L}_2 = 2\int_0^1 (1 - q^2)dq\Bigg[\frac{2\hat{\Sigma}_b}{\sqrt{(2 - q^2)(1 - (1 - q^2)^4\rho_m^4)}} - q\rho_m^2\hat{A}\frac{\sqrt{1 - (1 - q^2)^2}}{(1 - (1 - q^2)^4\rho_m^4)^{3/2}}\Bigg], \tag{2.25}$$

where again the components of the metric in the above expression are functions of (τ_0, ρ_0, x_*) with $\tau_0(q)$ and $\rho_0(q)$.

We can interpret the final Gaussian distribution that is produced at late times as a signal of a successful thermalization. Among the different simulations that have been performed in this section for parameters in the range of $\rho_m \in \{0.1\rho_h, 0.5\rho_h, 0.9\rho_h, 0.999\rho_h\}$,[9] those that correspond to $\rho_m = 0.9\rho_h - 0.999\rho_h$ could be verified to have reached the thermalization. Figures 3(a)–3(d) show the correlation between two fixed points in the y axes for

---

[9] For the rest of the simulations in the paper, we fixed $\rho_h = 1$.

different $\alpha \in \{1, \frac{1}{2}, \frac{1}{4}, \frac{1}{8}\}$ while a scalar field that has a Gaussian profile as a function of x is falling into the black hole in the bulk space. In these figures, different observers stationed on the x axis will measure the correlation between the two specific points on the y axes differently. The maximum correlation is measured on the $x = 0$ axis, and other measurements are symmetric around this axis as the original profile for $p_0(\tau, x)$ has this symmetry. As the quench is triggered, there appears a "phase transition" in a sense that the sign of the correlation function changes sign; from zero in the ground state, it goes to a minimum negative value and undoes itself and reaches a final saturated maximum. The rather simple form of Eq. (2.25) shows that this transition is due to the interplay between $\hat{\Sigma}_b$ and the warp factor $\hat{A}$. The first term is always positive, while the sign of the second term varies depending on the sign of $\hat{A}$. Reduction of the value of α makes the late-time Gaussian-like distribution disappear, signaling a fully thermalized equilibrium state measured by the observable in the universal (abrupt quench) limit.

In Figs. 4(a) and 4(b), we compare the effect of changing σ in the range $\sqrt{L_x} - \sqrt{1.5L_x}$. In the next section, we will compare these results with those of case II.

2. Case II: Plane C–D

In this section, we consider two-point correlations again, while we measure the inhomogeneity in a plane perpendicular to the one in the previous section. For an illustration, refer to Fig. 2 and the comments at the begging of that section. The relative geometry of the setup here is more important as it resembles the setup of the elliptic flow in heavy-ion collisions. In both cases, there are distributions that are localized in the transverse directions. Of course, the physics of the two cases are not directly related.

The effect of the backreaction on the coordinates will be parametrized by

$$\tau = \tau_0 + l^2 \tau_2, \quad \rho = \rho_0 + l^2 \rho_2, \quad x = x_0 + l^2 x_2. \tag{2.26}$$

In what follows, we will use x_0 to parametrize the geodesic. Expansion in terms of the above series will then yield:

the geodesic equation for $\boldsymbol{\tau}_2$:

$$\ddot{\tau}_2 + 2\frac{\dot{\tau}_0 \dot{\tau}_2}{\rho_0}(1 + \rho_0^4) - 2\frac{\dot{x}_2}{\rho_0} + \frac{\rho_2}{\rho_0^2}(1 - \dot{\tau}_0^2 + 3\dot{\tau}_0^2 \rho_0^4) - 2\frac{\hat{\Sigma}_d}{\rho_0} - \frac{1}{2}\dot{\tau}_0^2 \rho_0^2 \partial_\rho \hat{A} + \dot{\tau}_0 \rho_0^2 \partial_\rho \hat{\Xi}_f + \partial_\rho \hat{\Sigma}_d = 0, \tag{2.27}$$

the geodesic equation for $\boldsymbol{\rho}_2$:

$$\begin{aligned} &\ddot{\rho}_2 + 2\frac{\dot{x}_2}{\rho_0}(1 - \rho_0^4) - 2\dot{\rho}_2\left(\frac{\dot{\tau}_0}{\rho_0} + 2\frac{\dot{\rho}_0}{\rho_0} + \dot{\tau}_0 \rho_0^3\right) - 2\dot{\tau}_2\left(\frac{\dot{\tau}_0}{\rho_0} + \frac{\dot{\rho}_0}{\rho_0} + \dot{\rho}_0 \rho_0^3 - \dot{\tau}_0 \rho_0^7\right) \\ &+ \left(-\frac{1}{\rho_0^2} + \frac{\dot{\tau}_0^2 + 2\dot{\rho}_0^2 + 2\dot{\tau}_0 \dot{\rho}_0}{\rho_0^2} - 3\rho_0^2 - 6\dot{\tau}_0 \dot{\rho}_0 \rho_0^2 + 7\dot{\tau}_0^2 \rho_0^6\right)\rho_2 + \rho_0(1 - \dot{\tau}_0^2(1 + \rho_0^4))\hat{A} \\ &- 2\dot{\rho}_0 \rho_0 \Xi + \frac{2}{\rho_0}(1 - \rho_0^4)\hat{\Sigma}_d + \dot{\tau}_0 \rho_0^2 \partial_x A - \rho_0^2 \partial_x \hat{\Xi}_f + \frac{\dot{\tau}_0 \rho_0^2}{2}(\dot{\tau}_0 + 2\dot{\rho}_0 - \dot{\tau}_0 \rho_0^4)\partial_\rho \hat{A} \\ &+ \rho_0^2(-\dot{\tau}_0 - \dot{\rho}_0 + \dot{\tau}_0 \rho_0^4)\partial_\rho \hat{\Xi}_f + (-1 + \rho_0^4)\partial_\rho \hat{\Sigma}_d + \frac{1}{2}\dot{\tau}_0^2 \rho_0^2 \partial_\tau \hat{A} + \partial_\tau \hat{\Sigma}_d = 0, \end{aligned} \tag{2.28}$$

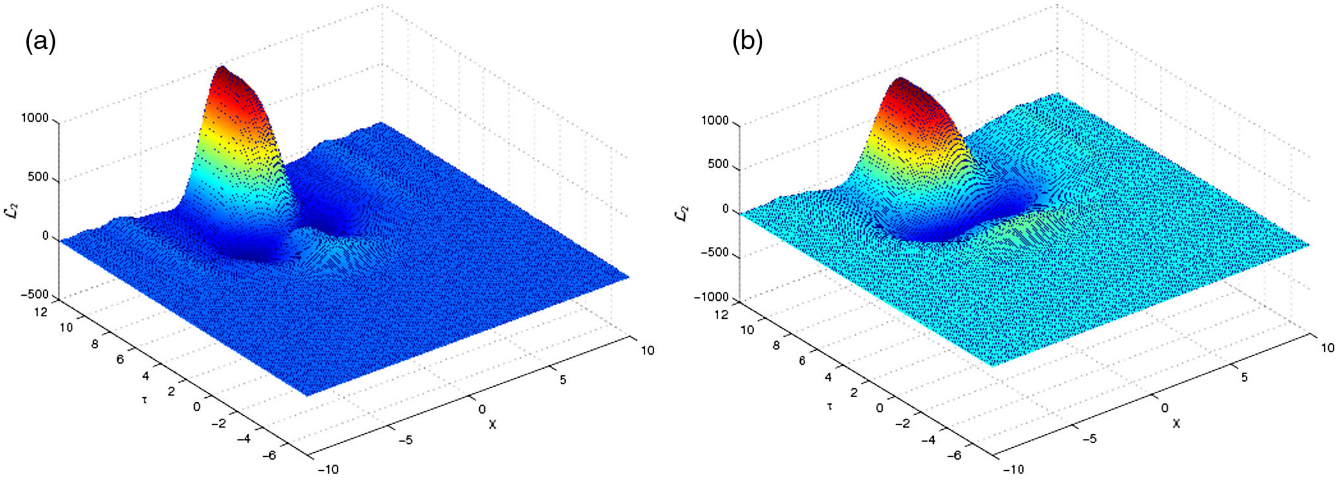

FIG. 4. Changing the value of σ from $\sqrt{L_x}$ to $\sqrt{1.5L_x}$ from left to right causes the distributions to rescale. This factor must be a nontrivial function of the dynamics under study. On the left-hand side $N_x = N_\rho = 20$ and on the right-hand side $N_x = N_\rho = 30$ Chebyshev points have been used.

the geodesic equation for $\boldsymbol{x}_2$:

$$\begin{aligned}&\ddot{x}_2-2\frac{\dot{x}_2\dot{\rho}_0}{\rho_0}-2\frac{\dot{\rho}_2}{\rho_0}+2\frac{\dot{\rho}_0\rho_2}{\rho_0^2}+\rho_0(1-\dot{\tau}_0^2(1+\rho_0^4))\hat{\Xi}_f\\&\quad+\frac{1}{2}\dot{\tau}_0^2\rho_0^2\partial_x\hat{A}+\partial_x\hat{\Sigma}_d+\dot{\tau}_0\dot{\rho}_0\rho_0^2\partial_\rho\hat{\Xi}_f+2\dot{\rho}_0\partial_\rho\hat{\Sigma}_d\\&\quad+\dot{\tau}_0^2\rho_0^2\partial_\tau\hat{\Xi}_f+2\dot{\tau}_0\partial_\tau\hat{\Sigma}_d=0,\end{aligned}\tag{2.29}$$

and we can verify that the geodesics on the y and z axes are not affected at $\mathcal{O}(l^2)$. The metric compatibility condition will subsequently change to

$$\begin{aligned}&\dot{x}_2-\dot{\tau}_0\dot{\rho}_2+(-\dot{\tau}_0-\dot{\rho}_0+\dot{\tau}_0\rho_0^4)\dot{\tau}_2\\&\quad+\frac{\rho_0}{\rho_2}(-1+\dot{\tau}_0^2+2\dot{\tau}_0\dot{\rho}_0+\dot{\tau}_0^2\rho_0^4)-\frac{1}{2}\dot{\tau}_0^2\rho_0^2A+\dot{\tau}_0\rho_0^2\Xi\\&\quad+\Sigma_d=0.\end{aligned}\tag{2.30}$$

Note the appearance of the disturbances in Eq. (2.28) for the bulk radius, and compare it to the previous case. This completes the list of the required geodesics which could have been driven otherwise from the action principle.

The length of the spacelike geodesic that connects points C and D on $(x_1=-x_m, y_1=0, z_1=0, \tau_1=\tau_*)$ and $(x_2=x_m, y_2=0, z_2=0, \tau_2=\tau_*)$ is given by

$$\mathcal{L}=\int_{-x_m}^{x_m}dx_0\sqrt{-A\dot{\tau}^2+\Sigma_d^2(1+\dot{x}_2)^2+2\Xi_f\dot{\tau}(1+\dot{x}_2)-2\frac{\dot{\rho}\,\dot{\tau}}{\rho^2}},\tag{2.31}$$

where in the above $\dot{\tau}=\dot{\tau}_0+l^2\dot{\tau}_2$, and we are assuming a similar expression for $\dot{\rho}$, too. In addition to $\rho(x_0)$, the metric components Σ_d, A and Ξ are functions of (τ,ρ,x_0) with $\tau(x_0)$ and $\rho(x_0)$. Expanding to $\mathcal{O}(l^2)$, at zeroth order, we find Eq. (2.18), and to the second order, it simplifies to

$$\begin{aligned}\mathcal{L}_2=&\int_{-x_m}^{x_m}\frac{dx_0}{\rho_0\sqrt{D}}\left(\hat{\Sigma}_d-\frac{1}{2}\dot{\tau}_0^2\hat{A}+\dot{\tau}_0\rho_0^2\hat{\Xi}_f\right)\\&+\int_{-x_m}^{x_m}\frac{dx_0}{\rho_0\sqrt{D}}\Bigg[\dot{x}_2-\dot{\tau}_0\dot{\rho}_2+(-\dot{\tau}_0-\dot{\rho}_0+\dot{\tau}_0\rho_0^4)\dot{\tau}_2\\&+\frac{-D+2\dot{\tau}_0^2\rho_0^4}{\rho_0}\rho_2\Bigg],\end{aligned}\tag{2.32}$$

with D defined in Eq. (2.20). Similar to case I, the equations of motion at zeroth order will allow us to simplify the above expression. The term proportional to $\dot{\tau}_2$ and the combination of the coefficients that multiply ρ_2 and $\dot{\rho}_2$ will cancel out. The only nonzero contribution from the second line of Eq. (2.32) comes from $\dot{x}_2$. The interpretation of this term is the following; we have chosen x_0 as a parameter that covers the geodesic between the two fixed points on the boundary, but this coordinate is also along the axis that the inhomogeneity is sourced accordingly by the profile of the scalar field. Therefore, this term compensates for the fact that we are constraining the geodesic in a fixed interval.

By partial integration and equations of motion, we can reduce the contribution to

$$\begin{aligned}\mathcal{L}_2=&\int_{-x_m}^{x_m}\frac{dx_0}{\rho_0\sqrt{D}}\left(\hat{\Sigma}_d-\frac{1}{2}\dot{\tau}_0^2\hat{A}+\dot{\tau}_0\rho_0^2\hat{\Xi}_f+\dot{y}_0\hat{\Sigma}_b\right)\\&+\frac{x_2}{\rho_0\sqrt{D}}\bigg|_{-x_m}^{x_m}.\end{aligned}\tag{2.33}$$

Now, if we assume $2x_m\gg 1$, this means $x_2=0$ at $\pm x_m$. In this case, there is no contribution from the second term in Eq. (2.33). While this is an interesting scenario, we pursue the general case and therefore do not impose this later boundary condition. Notice that splitting the integral into $\int_0^{x_m}$ would not help at all since in order to know the value of x_2 at $x_0=0$ we have to solve the geodesic equations all the way from the boundary down to the maximum value of the bulk radius.

First, we have to solve the equations of motion for τ_0 and ρ_0 in terms of x_0. They are already mentioned in Eq. (2.22) and Eq. (2.23). Choosing the positive root, the solution is given by

$$\frac{d\rho_0}{d\tilde{x}_0}=\frac{\sqrt{(1-\rho_0^4)(\rho_m^2-\rho_0^2)}}{\rho_0},\tag{2.34}$$

with the change of variable $\tilde{x}_0\equiv x_m-x_0$. Solving the above equation for $\tilde{x}_0$, in the limit of $\rho_0\to 0$, we find $\rho_0=\sqrt{2\rho_m\tilde{x}_0}$. From Eq. (2.23), we find $D=\frac{\rho_m}{2\tilde{x}_0}$, and therefore the denominator of the last term in Eq. (2.33) behaves as

$$\frac{1}{\rho_0\sqrt{D}}\sim\frac{1}{\rho_m},\tag{2.35}$$

which has a finite value. This means that imposing the boundary condition $x_2=0$ at $\pm x_m$ is safe and its contribution vanishes as the profile is symmetric around $x_0=0$. To write it in the final form, we use $\rho_0=\rho_m(1-q^2)$ and solve for $\dot{\tau}_0$ from Eq. (2.21) to obtain

$$\begin{aligned}\mathcal{L}_2=\int_0^1\frac{4(1-q^2)dq}{\sqrt{1-\rho_m^4(1-q^2)^4}}\Bigg(&\frac{\hat{\Sigma}_d}{\sqrt{2-q^2}}\\&-\frac{q^2\sqrt{2-q^2}}{2(1-q^2)^2(1-\rho_m^4(1-q^2)^4)}\hat{A}\\&+\frac{\rho_m^2q(1-q^2)}{\sqrt{1-\rho_m^4(1-q^2)^4}}\hat{\Xi}_f\Bigg).\end{aligned}\tag{2.36}$$

Similarly to the last section, plots for the above expression are shown in Figs. 5(a)–5(e) for various tuning parameters

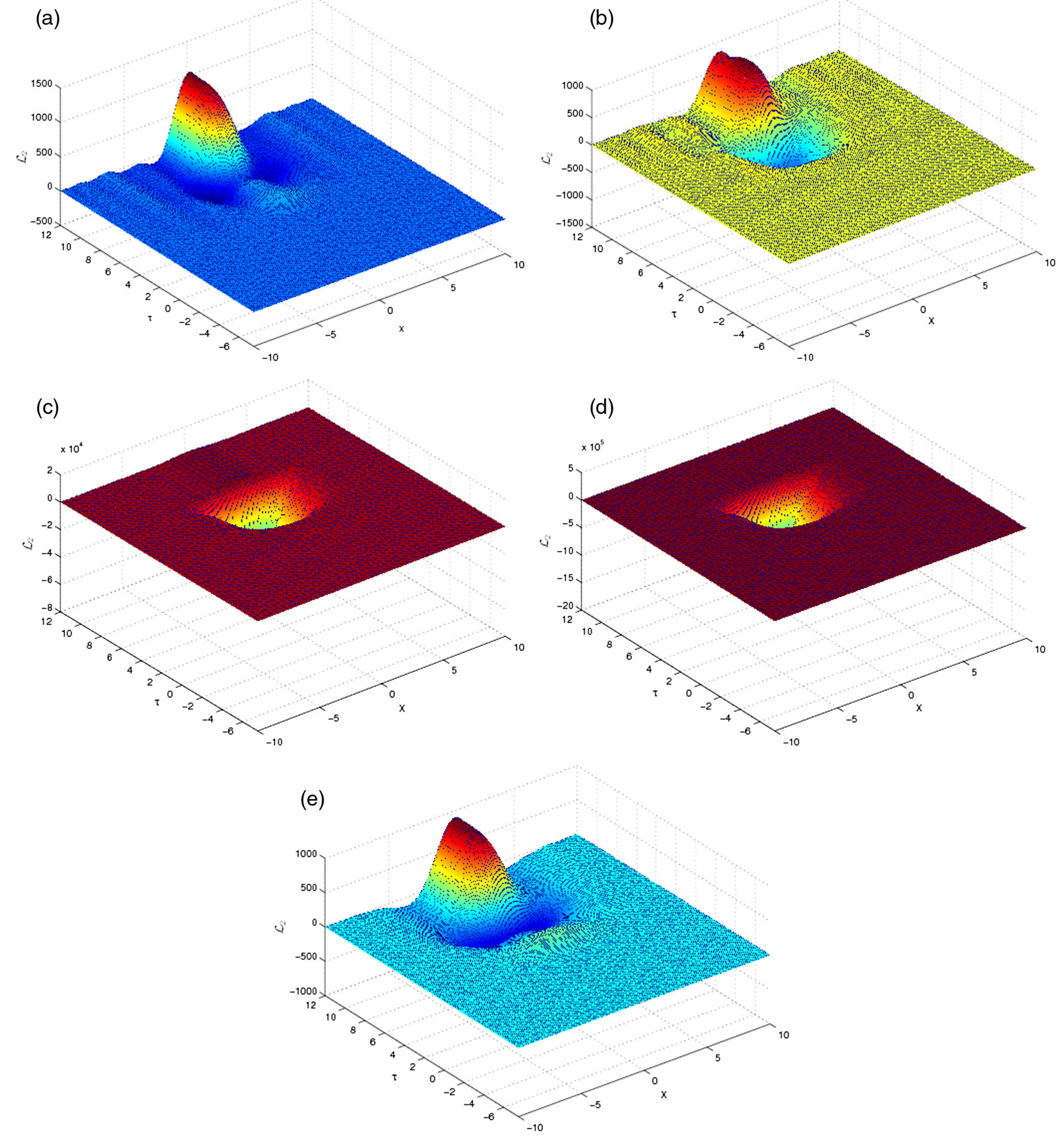

FIG. 5. Time evolution of the two-point Wightman function for operators with large conformal dimension. In case II, the correlations are measured by an observer along the plane of reactions. Plots in (a), (b), (c) and (d) are for a fixed value of $\sigma = \sqrt{L_x}$ while varying $\alpha \in \{1, \frac{1}{2}, \frac{1}{4}, \frac{1}{8}\}$. Instead, in (e), $\alpha = 1$ with $\sigma = \sqrt{1.5L_x}$. All these figures are deduced for geodesics with the deepest bulk penetration which is given by the choice $\rho_m = 0.999\rho_h$ in our setup. Other parameters of the simulations are similar to ones used in the previous sections.

α and σ in Eq. (1.8). In Figs. 5(a)–5(d), plots for $\alpha \in \{1, \frac{1}{2}, \frac{1}{4}, \frac{1}{8}\}$ are shown, and in Fig. 5(e), $\sigma = \sqrt{1.5L_x}$. An important observation is made by comparing our plots to those of the last section. In fact, they look very identical. Let us remind ourselves about the difference between case I in Figs. 3(a)–4(b) and case II with the figures listed below. In the first scenario, correlation between two points on the y axes is measured while a scalar field with a Gaussian profile falls into the black hole. The correlation between the points is found by computing the geodesic connecting these pair of points through the bulk. This means that as the scalar field ϕ is falling into the bulk, the excitations that are produced by the form of the profile will affect the length of the geodesic. The plane of the flow of these excitations are orthogonal to the plane where the geodesic is drawn. In case II, both the excitations of the scalar field and the geodesics are on the same plane. The resemblance of the two scenarios is very nontrivial, although we also have to remember that our results are valid for correlations of operators with large mass dimensions. A rough explanation is that in $\mathcal{L}_2$ in both cases apart from the geometrical factors that parametrize the geodesics, case I, the functional dependence is given by $\mathcal{L}_2(\hat{\Sigma}_b, \hat{A})$, while in case II, we have $\mathcal{L}_2(\hat{\Sigma}_d, \hat{A}, \hat{\Xi}_f)$. From our simulations, it was clear that $\hat{\Sigma}_{d,b}$ were roughly at the same order, while $\hat{\Xi}_f \ll 1$. Notice also that $\hat{\Xi}_f$ is an odd function of x; this means that the plots in Figs. 5(a)–5(e) are not completely symmetric along $x = 0$ compared to those mentioned in Figs. 3(a)–4(b) of case I. For a similar conclusion on the connection between inhomogeneity and the appearance of odd functionalities in the correlation functions, refer to Ref. [28].

In the next section, we study entanglement entropies and show that they are more distinctive when it comes to different setups for thermalization.

C. Entanglement entropy

In this section, we generalize our previous arguments on two-point functions. Among different options for the minimal surfaces that one can use, we restrict ourselves to the strip geometry. Then, rather than probing the bulk by a single geodesic, we will measure the thermalization by a minimal surface that satisfies the boundary of a strip. We will follow Ryu and Takayanagi's [29] prescription for calculating the EE for holographic theories, which is based on extremizing bulk surfaces. For related works on EE, refer to Ref. [30].

1. Case I: Plane A–B

One natural way to parametrize the boundary is to use the set of coordinates (x, y, z). Let us parametrize the direction that forms an arc by going through the bulk to be y_0. Then, the geometry is extended indefinitely along the x and z axes. The situation that these two coordinates are cyclic has been considered recently in Ref. [20]. As before, we assume that the inhomogeneity backreacts along the x direction while leaving ∂_z as the Killing vector. The reader who is familiar with the derivations can skip to the discussion at the end of this subsection.

The surface area will be evaluated from the induced metric using coordinates (x, y, z). The induced metric to the hypersurface is conveniently derived by confining line elements to displacements confined to the hypersurface. Doing so, we find that

$$S_\Sigma = \int_{-\infty}^{\infty} dx_0 \int_{-\infty}^{\infty} dz_0 \int_{-y_m}^{y_m} dy_0 \sqrt{\gamma_{\mathrm{ind}}} \Sigma_b, \tag{2.37}$$

with tangent vectors of the curves on the hypersurface defined by $e^\alpha_a \equiv \frac{dx^\alpha}{dy^a}$ and

$$\begin{aligned}\gamma_{\mathrm{ind}} = {}& -2\frac{A}{\rho^2} e^\tau_x e^\tau_y (e^\tau_y e^\rho_x + e^\tau_x e^\rho_y) - 3A^2 (e^\tau_x e^\tau_y)^2 \\ & - \frac{2}{\rho^2}(e^\tau_x e^\rho_x \Sigma_b^2 + e^\tau_y e^\rho_y \Sigma_d^2) + \Sigma_b^2 \Sigma_d^2 \\ & + 2\Xi\left(3A e^\tau_x (e^\tau_y)^2 + 2\frac{(e^\tau_y)^2 e^\rho_x}{\rho^2} + e^\tau_x \Sigma_b^2\right) \\ & + 4\frac{e^\tau_x e^\tau_y e^\rho_x e^\rho_y}{\rho^4} - 4(e^\tau_y)^2 \Xi^2 \\ & - A[(e^\tau_y \Sigma_d)^2 + (e^\tau_x \Sigma_b)^2]. \end{aligned} \tag{2.38}$$

The equations of motion follow by varying the action

$$\partial_i \frac{\partial S_\Sigma}{\partial(\partial_i \tau)} - \frac{\partial S_\Sigma}{\partial \tau} = 0, \qquad \partial_i \frac{\partial S_\Sigma}{\partial(\partial_i \rho)} - \frac{\partial S_\Sigma}{\partial \rho} = 0, \tag{2.39}$$

with $i \in \{x, y\}$. Expanding the coordinates to $\mathcal{O}(l^2)$, the EE similar to the two-point Wightman functions, will have an expansion of the form $S_\Sigma = S_{\Sigma(0)} + l^2 S_{\Sigma(2)} + l^2 \delta S_{\Sigma(0)}$. To zeroth order in the perturbation, one gets for the hypersurface

$$S_{\Sigma(0)} = 2K^2 \int_0^{y_m} dy_0 \frac{\sqrt{D}}{\rho_0^3}, \tag{2.40}$$

where since the effect of the inhomogeneity comes from the backreaction of the metric and hence it is a $\mathcal{O}(l^2)$ effect, it will consequently be absent here and the integral over x will be done trivially. The cutoff K has been introduced for trivial integrations.

To second order, we have

$$\begin{aligned} S_{\Sigma(2)} = 2K \int_{-\infty}^{\infty} dx_0 \int_0^{y_m} dy_0 \frac{1}{2\rho_0^3 \sqrt{D}} \\ \times [2\hat{\Sigma}_b + 2(\hat{\Sigma}_b + \hat{\Sigma}_d)D - \dot{\tau}_0^2 \rho_0^2 \hat{A}]; \end{aligned} \tag{2.41}$$

also note that in the above expression, the integral over the coordinate x is now nontrivial as all the metric components $\hat{\Sigma}_b$, $\hat{\Sigma}_d$ and $\hat{A}$ are the backreacted corrections. The next contribution changes the boundary volume since it depends on τ_2, ρ_2 and x_2 according to

$$\delta S_{\Sigma(0)} = 2K \int_{-\infty}^{\infty} dx_0 \int_0^{y_m} dy_0 \times \left[\frac{2\dot{\tau}_0^2 \rho_0^4 - 3D}{\rho_0^4 \sqrt{D}} \rho_2 - \frac{\dot{\tau}_0}{\rho_0^3 \sqrt{D}} \dot{\rho}_2 - \frac{\dot{\tau}_0(1-\rho_0^4) + \dot{\rho}_0}{\rho_0^3 \sqrt{D}} \dot{\tau}_2 \right]. \tag{2.42}$$

It should be pointed out that if we assume $\dot{x}_0 \neq 0$, then a term proportional to x_2 will appear in the EE contribution. Similar to the previous case, looking at the geodesics will provide us the following equations for the profiles of $\rho_0(y)$ [20],

$$(1-\rho_0^4)\dot{\tau}_0 + \dot{\rho}_0 = 0, \qquad D\rho_0^6 = \rho_m^6, \tag{2.43}$$

which reduce to

$$\frac{d\rho_0}{dy} = -\frac{\sqrt{(1-\rho_0^4)(\rho_m^6 - \rho_0^6)}}{\rho_0^3}. \tag{2.44}$$

Although a full analytic solution to the above equation will be desirable, it suffices to find an asymptotic solution which will be required in the subsequent section,

$$y_0 = y_* - \frac{\rho_0^4}{4\rho_m^3} + \mathcal{O}(\rho_0^8); \tag{2.45}$$

this is the boundary coordinate as seen from an observer falling deep in the bulk. The straight substitution from Eq. (2.43) and Eq. (2.44) has shown that [20]

$$S_{\Sigma(0)} = 2K^2 \int_{\epsilon}^{\rho_m} d\rho_0 \frac{\rho_m^3}{\rho^3 \sqrt{(1-\rho^4)(\rho_m^6 - \rho^6)}}, \tag{2.46}$$

$$S_{\Sigma(2)} = 2K \int_{-\infty}^{\infty} dx_0 \int_0^{\rho_m} d\rho_0 \left[\frac{2\rho_0^6(1-\rho_0^4)\hat{\Sigma}_b + 2\rho_m^6(1-\rho_0^4)(\hat{\Sigma}_b + \hat{\Sigma}_d) - \rho_0^2(\rho_m^6 - \rho_0^6)\hat{A}}{2\rho_0^3\rho_m^3(1-\rho_0^4)^{3/2}\sqrt{\rho_m^6 - \rho_0^6}} \right]. \tag{2.47}$$

From Eq. (2.42), it is evident that we can simplify the expression using the equations of motion. The coefficients of $\ddot{\tau}_0$ cancel out. The derivative over $\dot{\rho}_2$ can be rewritten using the partial derivative in terms of ρ_2 which will be again proportional to the equations of motion. The only contribution emerging from the surface term is

$$\delta S_{\Sigma(0)} = 2K^2 \frac{\dot{\tau}_0}{\rho_0^3 \sqrt{D}} \rho_2 \Big|_0^{y_m}. \tag{2.48}$$

It is easiest first to evaluate the coefficient of ρ_2 because it is at zeroth order in the backreaction rather than calculating the whole expression. Since only the quantities such as $\dot{\tau}_0$ and $\dot{\rho}_0$ are required, we can expand around $y = 0$, which is equivalent to the top of the arc in the bulk where it gets its maximum value ρ_m. Perturbatively solving the equation of motion in Eq. (2.44), we obtain the following solutions:

$$\rho_0(y) = \rho_m + \frac{3}{2}\left(\frac{-1+\rho_m^4}{\rho_m}\right) y^2, \qquad \tau_0(y) = \frac{3}{2}\frac{y^2}{\rho_m}. \tag{2.49}$$

There is also a nonphysical solution $\rho_0(y) = \rho_m$ and $\tau_0(y) = \frac{3}{2}\frac{y^2}{\rho_m}$; this solution can be discarded as it takes an infinite amount of time for the geodesic to satisfy the boundary condition. Nonetheless, both solutions give a vanishing contribution to the value of the expression in which we are interested.

The value of the expression at $y_0 = y_m$ requires more work. Since the boundary time τ_* will be the time at which $\rho_0 \to 0$, we can solve the differential equation in Eq. (2.44) to obtain $\rho_0 \sim (y_m - y_0)^{1/4}$. Putting everything together [20], we obtain the coefficient of $\rho_2(y_0)$,

$$-2K \frac{1}{2\sqrt{2}\rho_m^{9/4}\delta^{3/4}}, \tag{2.50}$$

where in the above δ is a regulator to avoid the singularity of the upper limit of $y = y_m$. As has been argued, one needs to evaluate the behavior of $\rho_2(y_0)$ to find the finite contribution to the entanglement entropy. Following the method described in Ref. [20], we vary the action in Eq. (2.37) for $\tau_2(y_0)$ and $\rho_2(y_0)$ as it is not clear from the beginning whether or not there will be a modification from terms that depend on the inhomogeneity in the action of Eq. (2.37). From the Euler-Lagrange equations

$$\delta_{\rho_2} S_\Sigma - \frac{d}{dy_0}(\delta_{\dot{\rho}_2} S_\Sigma) = 0, \quad \delta_{\tau_2} S_\Sigma - \frac{d}{dy_0}(\delta_{\dot{\tau}_2} S_\Sigma) = 0, \tag{2.51}$$

at $\mathcal{O}(l^2)$, naturally, we recover the equations of motion for the unperturbed variables ρ_0 and τ_0. Along the same line, at $\mathcal{O}(l^4)$, we find the equations of motion for τ_2 and ρ_2. These are *ab initio* nonlinear equations involving components of metric A, Σ_b, Σ_d and Ξ on one hand and τ_0, ρ_0, τ_2 and ρ_2 on the other. As the singularity in Eq. (2.50) originates from the limit of $\rho \to 0$, we can replace the components of the metric with their leading values in Eq. (A18)–Eq. (A21) from the Appendix. Using the asymptotic expansions for τ_0 and ρ_0 as mentioned in the paragraph above Eq. (2.50), at leading order, we find

$$\ddot{\rho}_2 + \ddot{\tau}_2 = \frac{1}{24\sqrt{2}} \frac{\rho_m^{9/2} p_0^2(\tau_*, x_*)}{\tilde{y}_0^{5/4}} + \mathcal{O}(1/\tilde{y}_0), \tag{2.52}$$

where in the above $\tilde{y}_0 = (y_m - y)$. In the limit of $\tilde{y}_0 \to 0$, assuming the derivatives of p_0 are suppressed by extra factors of $\tilde{y}_0$, the former degenerate equation [20] yields

$$\rho_2 + \tau_2 = -\frac{\sqrt{2}}{9} p_0^2(\tau_*, x_*) \rho_m^{9/2} \delta^{3/4}. \tag{2.53}$$

Since there is no modification from the other components of the metric, this is identical to the homogeneous case in Ref. [20]. Finding the coefficient will result in

$$\delta S_{\Sigma(0)} = K^2 \frac{5}{36} p_0^2(\tau_*, x_*). \tag{2.54}$$

The integral in Eq. (2.47) is singular at $\rho_0 = 0$, and we have to regularize it. To do so, as before, we make use of the asymptotic expansions of the metric components for $\rho_0 \to 0$ in Eq. (A18)–Eq. (A20),

$$\hat{A} = -\frac{1}{6} p_0^2 + \rho_0^2 a_2 + \mathcal{O}(\rho_0^2 \ln \rho_0), \tag{2.55}$$

$$\hat{\Sigma}_d = -\frac{1}{12} \rho_0^2 p_0^2 + \rho_0^4 d_4 + \mathcal{O}(\rho_0^4 \ln \rho_0), \tag{2.56}$$

$$\hat{\Sigma}_b = -\frac{1}{12} \rho_0^2 p_0^2 + \rho_0^4 b_4 + \mathcal{O}(\rho_0^4 \ln \rho_0); \tag{2.57}$$

then, from the expansion around the singularity, a counterterm can be formed,

$$S_{\text{counter}} = \frac{K^2}{6} p_0^2(\tau_*, x_*) \int_{\epsilon}^{\rho_m} \frac{d\rho_0}{\rho_0}, \tag{2.58}$$

where ϵ is a regulator for the integral. Substituting from Eq. (2.55)–Eq. (2.57), the finite part of Eq. (2.47) reads

$$S_{\Sigma(2)}^{\text{fin}} = 2K \int_{-\infty}^{\infty} dx_0 \int_0^{\rho_m} \rho_0 d\rho_0 \left[\frac{2\rho_0^6(1-\rho_0^4) b_4 + 2\rho_m^6 (1-\rho_0^4)(b_4 + d_4) - (\rho_m^6 - \rho_0^6) a_2}{2\rho_m^3 (1-\rho_0^4)^{3/2} \sqrt{\rho_m^6 - \rho_0^6}} \right],$$

with a_2, b_4 and d_4 functions of (τ_0, x_0) with $\tau_0(\rho_0)$. The corresponding divergent part evaluates to

$$S_{\Sigma(2)}^{\text{div}} = -2K \int_{-\infty}^{\infty} dx_0 \int_{\epsilon}^{\rho_m} d\rho_0 \frac{p_0^2(\tau_0, x_0)}{12} \left[\frac{2\rho_0^6(1-\rho_0^4) + 4\rho_m^6(1-\rho_0^4) - 2(\rho_m^6 - \rho_0^6)}{2\rho_0 \rho_m^3 (1-\rho_0^4)^{3/2} \sqrt{\rho_m^6 - \rho_0^6}} \right].$$

Now, it is convenient to make the process of regularization scheme independent by adding

$$S_{\text{cor}} = -\frac{K^2}{6} p_0^2(\tau_*, x_*) \log \rho_m. \tag{2.59}$$

Finally, the total entanglement entropy for the strip geometry, including the inhomogeneity implicitly, will be

$$\begin{aligned} S_{\Sigma(2)} &= S_{\Sigma(2)}^{\text{fin}} + S_{\Sigma(2)}^{\text{div}} + S_{\text{counter}} + S_{\text{cor}} + \delta S_{\Sigma(0)} \\ &= 4K \int_{-\infty}^{\infty} dx_0 \int_0^1 q dq \left[\frac{\rho_m^2 (1-q^2)^7 b_4}{\sqrt{(1-\rho_m^4(1-q^2)^4)(1-(1-q^2)^6)}} + \frac{\rho_m^2 (1-q^2)(b_4 + d_4)}{\sqrt{(1-\rho_m^4(1-q^2)^4)(1-(1-q^2)^6)}} \right. \\ &\quad - \frac{\rho_m^2 (1-q^2) \sqrt{1-(1-q^2)^6}\, a_2}{2(1-\rho_m^4(1-q^2)^4)^{3/2}} - \frac{(1-q^2)^5 p_0^2(\tau_0, x_0)}{12\rho_m \sqrt{(1-\rho_m^4(1-q^2)^4)(1-(1-q^2)^6)}} \\ &\quad \left. - \frac{p_0^2(\tau_0, x_0)}{6\rho_m (1-q^2) \sqrt{(1-\rho_m^4(1-q^2)^4)(1-(1-q^2)^6)}} + \frac{p_0^2(\tau_0, x_0) \sqrt{1-(1-q^2)^6}}{12\rho_m (1-q^2)(1-\rho_m^4(1-q^2)^4)^{3/2}} \right] \\ &\quad + \frac{K^2}{6} p_0^2(\tau_*, x_*) \left[\int_0^1 \frac{2q dq}{1-q^2} - \log \rho_m + \frac{5}{6} \right]. \end{aligned} \tag{2.60}$$

Note the difference between $p_0(\tau_0, x_0)$ and $p_0(\tau_*, x_*)$. They will have some overlap in their values when they cover the spacetime with $\tau_0(q)$ but in general are independent. The fact that the metric components $a_2(\tau_0, x_0)$, $b_4(\tau_0, x_0)$ and $d_4(\tau_0, x_0)$ are nonlinear functions of the inhomogeneity makes Eq. (2.60) a nontrivial generalization of the result in Ref. [20].

EE as a local observable provides more detailed information for thermalization compared to other observables that we have studied so far. First, we plan to study its dependence on the cutoff ρ_m that we have chosen in our analysis. Figure 6(a) is the profile of $p_0(\tau, x)$, the non-normalizable mode of the scalar field, which is falling into the black hole. Figures 6(b)–6(e) are the corresponding variations of the EE as a function of the coordinates $x - \tau$ as we increase the value of the maximum depth of the entangling surface into the bulk from $0.1\rho_m$ to $0.999\rho_m$. This has the effect of shifting the amplitudes toward more positive values. It is easy to see from Eq. (2.60) that the dynamics of EE for $\rho_m \ll 1$ is dominated by the original profile of $p_0(\tau, x)$ in addition to a constant offset contribution for $\tau < 0$. At $\rho_m \sim 1$, this dynamics will be dominated by the backreacted components of the metric instead. This also explains why in Fig. 6(e) the early Gaussian peak that appears at $\tau \simeq 0$ is wider than the same Gaussian peak at late times due to the sudden appearance of the mass gap and plethora of excitations that follow. Figure 6(e) is the closest configuration to a realistic thermalization.

Our EE expressions are complicated, and they do not show the simple quasiparticle picture proposed by Cardy *et al.* [7,8]. Nevertheless, we can still connect to this idea. As it is shown in Figs. 7(a)–7(c), we vary the tuning parameter $\alpha \in \{\frac{1}{2}, \frac{1}{4}, \frac{1}{8}\}$. While we reduce the values of α, the mass gap production will have a steep slope. This in part causes more excitations per volume. These "quasiparticles" are constrained by causality and from a given Cauchy surface at $\tau = 0$; it will take them $\tau = x/v_{\max}$ to reach to their "horizon." This effect can be seen in Fig. 7(c) in a very pronounced way as it makes a slight wiggle on the surface at $\tau \sim 5$.

In Figs. 7(d), 7(e) and 7(f), we are gradually increasing the width of the Gaussian profile for $p_0(\tau, x)$. This causes the blue region (in color), surrounding the bump, to shift toward the negative values and to expand the width of the peak at $\tau = 0$. Curiously, this latter effect does not exceed a circular-shape region obeying radius $\tau = x/v_{\max}$. We want to point out that this is not trivial.

2. Case II: Plane C–D

Similar to the case considered in Sec. II B 2, for the two-point function, we reconsider a similar problem assuming that the direction of the inhomogeneity is orthogonal to the boundaries of the entangling region. Let us call this region A. The geometry of A is that of a strip, and we parametrize it with (x_0, y_0, z_0). The extremal surface that bounds A throughout the bulk is derived from

$$S_\Sigma = \int_{-\infty}^{\infty} dy_0 \int_{-\infty}^{\infty} dz_0 \int_{-x_m}^{x_m} dx_0 \sqrt{\gamma_{\text{ind}}} \Sigma_b^2, \tag{2.61}$$

with

$$\gamma_{\text{ind}} = -A\dot{\tau}^2 + 2\dot{\tau}(1+\dot{x}_2)\Xi + (1+\dot{x}_2)^2\Sigma_d^2 - 2\frac{\dot{\tau}\dot{\rho}}{\rho^2}, \tag{2.62}$$

and the boundary for the hypersurface (strip) is from $-x_m$ to x_m, and it is indefinitely extended along the y and z directions. Note that in writing Eq. (2.61), we relied on the lessons learned from the geodesic equations mentioned at the beginning such as Eq. (2.29). Expansion has the general form $S_\Sigma = S_{\Sigma(0)} + l^2 S_{\Sigma(2)} + l^2 \delta S_{\Sigma(0)}$. The first term has already been calculated in Eq. (2.40). For $S_{\Sigma(2)}$, we get

$$S_{\Sigma(2)} = 2K^2 \int_0^{x_m} \frac{dx_0}{2\rho_0^3\sqrt{D}} \times (2\hat{\Xi}_f \dot{\tau}_0 \rho_0^2 - \dot{\tau}_0{}^2 \rho_0^2 \hat{A} + 4D\hat{\Sigma}_b + 2\hat{\Sigma}_d), \tag{2.63}$$

with $D = 1 - \dot{\tau}_0{}^2 + \dot{\tau}_0{}^2\rho_0^4 - 2\dot{\tau}_0\dot{\rho}_0$. A similar expansion for the dynamical variables such as τ_2, ρ_2 and x_2 gives

$$\delta S_{\Sigma(0)} = 2K^2 \int_0^{x_m} \frac{dx_0}{2\rho_0^4\sqrt{D}} [2\rho_0\dot{x}_2 + (-6D + 4\dot{\tau}_0^2\rho_0^4)\rho_2 - 2\rho_0(\dot{\tau}(1-\rho_0^4) + \dot{\rho})\dot{\tau}_2 - 2\rho_0\dot{\tau}_0\dot{\rho}_2]. \tag{2.64}$$

As was noticed in the last section, the coefficient of $\dot{\tau}_2$ is zero if we use the equations of motion at zeroth order. Again, the coefficient of the terms ρ_2 and $\dot{\rho}_2$ group together by partial integrations, yielding

$$\delta S_{\Sigma(0)} = 2K^2 l^2 \frac{\dot{\tau}_0\rho_2}{\rho_0^3\sqrt{D}}\bigg|_0^{x_m} + K^2 l^2 \frac{x_2}{\rho_0^3\sqrt{D}}\bigg|_{-x_m}^{x_m}, \tag{2.65}$$

where in the above we applied the equations of motion such as Eq. (2.43). In addition, we have changed the lower bound of the second term as we explained below Eq. (2.33). They are both diverging with $\delta^{-3/4}$ where δ is the cutoff in the x_0 direction when ρ_0 approaches the boundary. The first term is identical to the contribution from the surface term in case I, but the second term is new and is due to the effect of the inhomogeneity. It is also challenging since if we want to enforce the boundary condition of $x_2 = 0$ at $\pm x_m$ the coefficient must be finite. To find the exact value of the coefficient, we have to solve for the equations of motion for x_2 close to the boundary.

Using the fact that $\rho_0 \sim (x_m - x_0)^{1/4}$ and the boundary expansions to leading order for the metric coefficients, such as

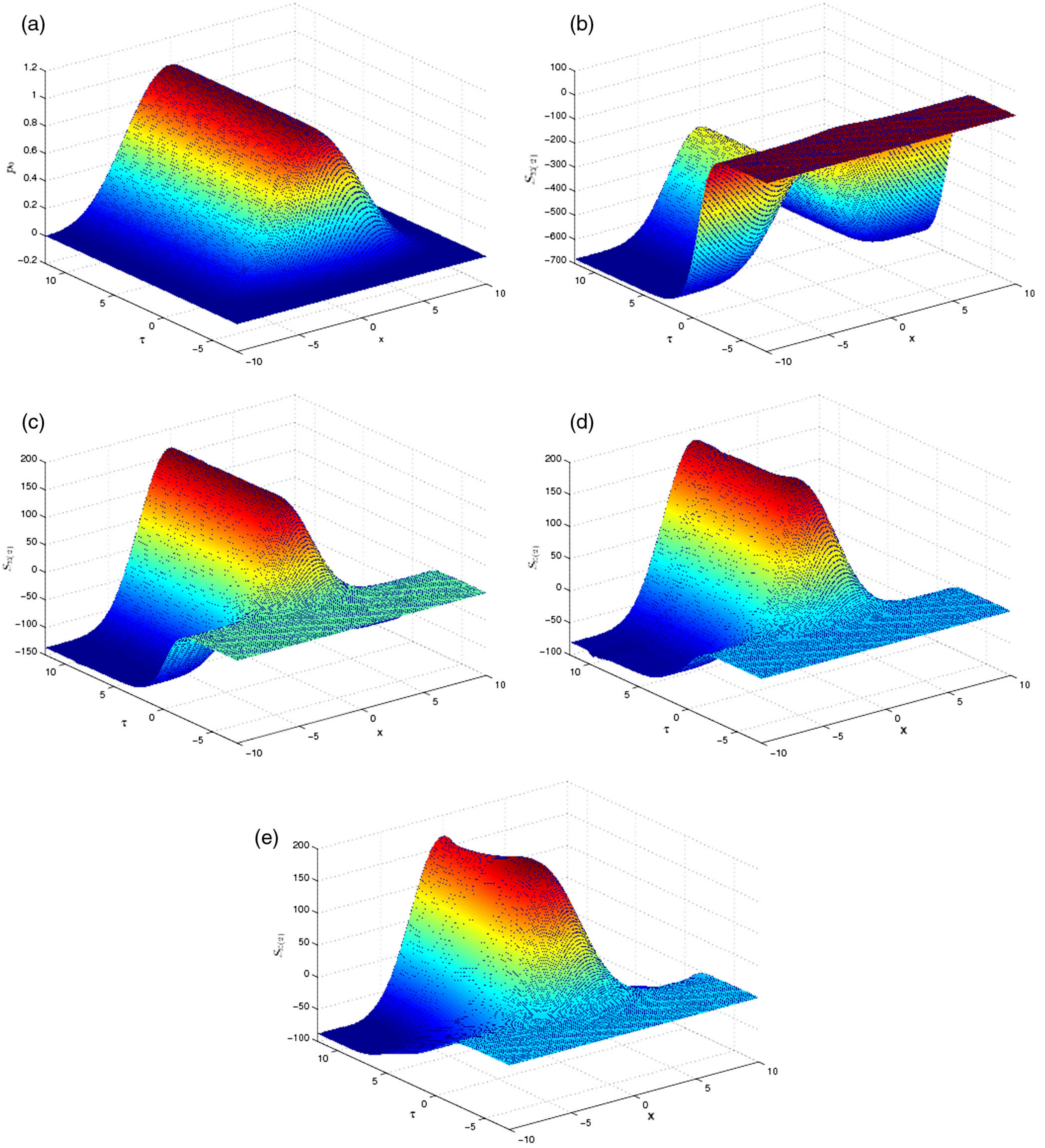

FIG. 6. Plots of the time evolution of the variation of the entanglement entropy at $\mathcal{O}(l^2)$. In case I, the correlating region is orthogonal to the plane of reaction. (a) is the source on the boundary, and (b)–(e) are the corresponding plots for the EE as we vary ρ_m for fixed $\alpha = 1$ and $\sigma = L_x$. The numerical setup is identical to the previous sections.

$$\hat{\Sigma}_b = -\frac{\rho_0^2}{12} p_0^2(\tau_0, x_0) + \mathcal{O}(\rho_0^4), \tag{2.66}$$

$$\hat{\Sigma}_d = -\frac{\rho_0^2}{12} p_0^2(\tau_0, x_0) + \mathcal{O}(\rho_0^4), \tag{2.67}$$

$$\hat{\Xi}_f = -\frac{\rho_0}{9} p_0(\tau_0, x_0) \frac{\partial p_0(\tau_0, x_0)}{\partial x_0} + \mathcal{O}(\rho_0^2), \tag{2.68}$$

$$\hat{A} = -\frac{1}{6} p_0^2(\tau_0, x_0) + \mathcal{O}(\rho_0^2), \tag{2.69}$$

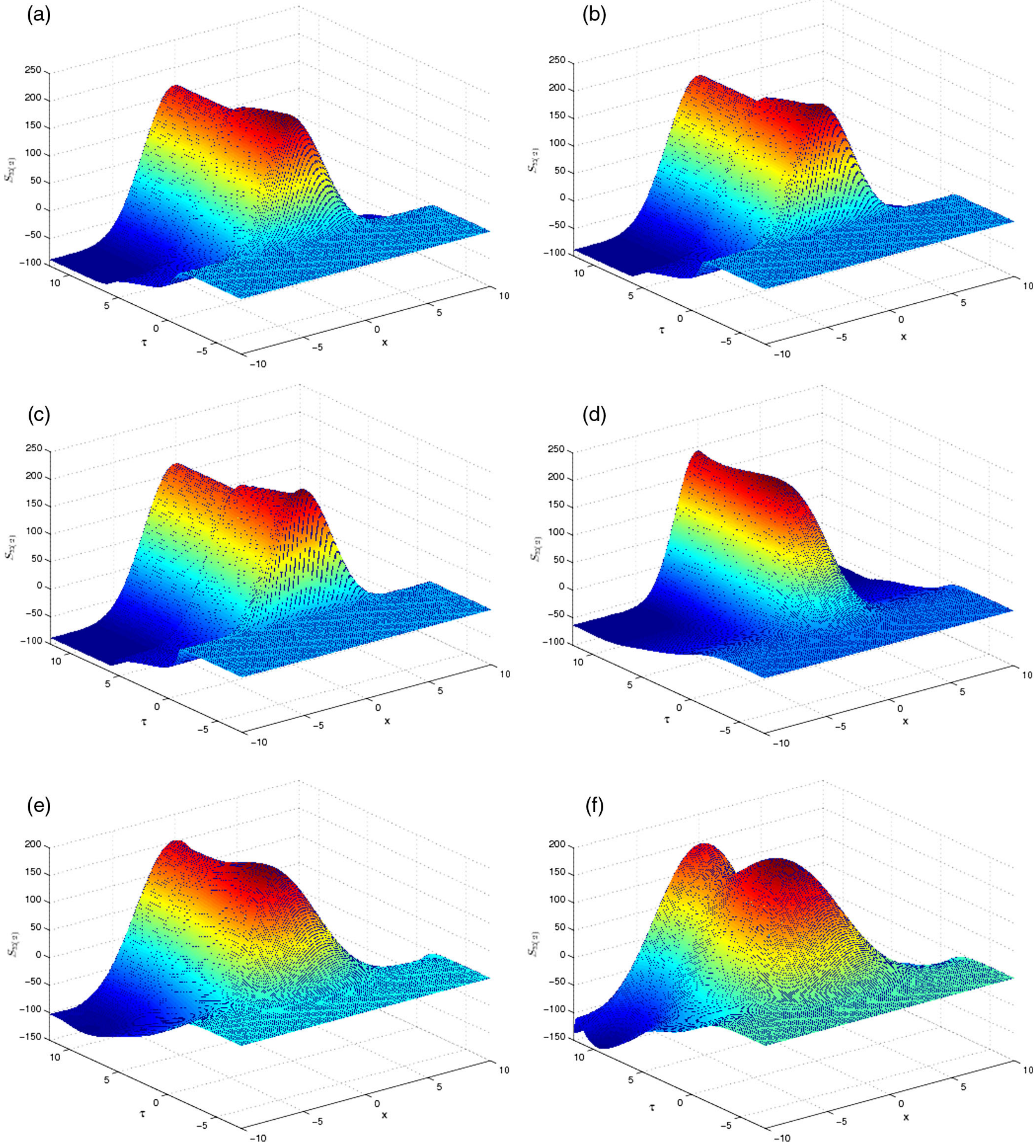

FIG. 7. Corresponding plots for the EE as we reduce α in (a)–(c) for $\sigma = \sqrt{L_x}$. In (d)–(f), we increase σ with fixed $\alpha = 1$. We are also assuming $\rho_m = 0.999\rho_h$ and $L_x = 10$ in the above plots.

together with the equations of motion derived from the Euler-Lagrange equations

$$\delta_{\rho_2} S_\Sigma - \frac{d}{dx}(\delta_{\dot{\rho}_2} S_\Sigma) = 0, \tag{2.70}$$

$$\frac{d}{dx}(\delta_{\dot{\tau}_2} S_\Sigma) = 0, \tag{2.71}$$

$$\frac{d}{dx}(\delta_{\dot{x}_2} S_\Sigma) = 0, \tag{2.72}$$

we find the following geodesic equations around the boundary surface[10]:

$$\ddot{\rho}_2 + \ddot{\tau}_2 = \frac{1}{24\sqrt{2}} \frac{\rho_m^{9/2} p_0^2(\tau_*, x_*)}{\tilde{y}_0^{5/4}}, \tag{2.73}$$

$$4\ddot{x}_2 - \frac{2\sqrt{2}}{\rho_m^{3/4}} \tilde{x}_0^{3/4} \ddot{\rho}_2 - \frac{3\sqrt{2}}{\rho_m^{3/4}} \frac{\dot{\rho}_2}{\tilde{x}_0^{1/4}} + \frac{3}{4\sqrt{2}} \frac{\rho_2}{\tilde{x}_0^{5/4}} = \frac{5\rho_m^{3/2}}{12} \frac{p_0^2(\tau_*, x_*)}{\tilde{x}_0^{1/2}}. \tag{2.74}$$

Therefore, in this case, we recover the degenerate equations of motion for $\ddot{\rho}_2$ and $\ddot{\tau}_2$ and an extra equation of motion for $\ddot{x}_2$. The same coefficients that have been obtained in the limit of long late times, that is $p_0 \to \text{const.}$, should be valid in this case and will allow us to determine $\ddot{x}_2$. An easy power counting shows that $x_2 \sim \tilde{x}_0^{3/2}$. If we insert the value of ρ_2 given at the late-time approximation when the system has reached thermalization [20], we find $\ddot{x}_2 = 0$. In either case, this means that the contribution from x_2 in Eq. (2.65) vanishes. Thus, the contribution from $\delta S_{\Sigma(0)}$ reads

$$\delta S_{\Sigma(0)} = \frac{5K^2}{36} p_0^2(\tau_*, x_*). \tag{2.75}$$

The contribution form the lower bound of the first term in Eq. (2.65) vanishes as the reader can easily check from the zeroth-order equations of motion. Going back to Eq. (2.63) and making a change of variable from x_0 to ρ_0 using Eq. (2.43) and Eq. (2.44) and renaming y_0 for x_0, we obtain

$$S_{\Sigma(2)} = K^2 \int_0^{\rho_m} \frac{\rho_0^3 d\rho_0}{\rho_m^3 \sqrt{(1-\rho_0^4)(\rho_m^6-\rho_0^6)}} \left[\frac{2}{\rho_0} \left(\frac{\rho_m^6 - \rho_0^6}{1-\rho_0^4} \right)^{1/2} \hat{\Xi}_f - \frac{\rho_m^6 - \rho_0^6}{\rho_0^4(1-\rho_0^4)} \hat{A} + \frac{4\rho_m^6}{\rho_0^6} \hat{\Sigma}_b + 2\hat{\Sigma}_d \right]. \tag{2.76}$$

As is clear from the above expression, it suffers from infrared divergences. To separate them from the finite part, we use the asymptotic expansion around the boundary using Eq. (A18)–Eq. (A21) in the Appendix,[11] i.e.

$$A = -\frac{p_0^2}{6} + \rho_0^2 a_2 + \mathcal{O}(\rho_0^2 \ln \rho_0), \tag{2.77}$$

$$\Sigma_d = -\rho_0^2 \frac{p_0^2}{12} + \rho_0^4 d_4 + \mathcal{O}(\rho_0^4 \ln \rho_0), \tag{2.78}$$

$$\Sigma_b = -\rho_0^2 \frac{p_0^2}{12} + \rho_0^4 b_4 + \mathcal{O}(\rho_0^4 \ln \rho_0), \tag{2.79}$$

$$\Xi = -\rho_0 \frac{p_0 \partial_x p_0}{9} + \rho_0^2 f_2 + \mathcal{O}(\rho_0^2 \ln \rho_0), \tag{2.80}$$

to find the finite contribution,

$$S_{\Sigma(2)}^{\text{fin}} = K^2 \int_0^{\rho_m} \frac{d\rho_0}{18\rho_m^3(-1+\rho_0^4)^2(\rho_0^6-\rho_m^6)} \Big[-36 f_2 \rho_0^4 (-1+\rho_0^4)(\rho_0^6-\rho_m^6) - 4p_0' p_0 (1-\rho_0^4)^{3/2} (\rho_m^6-\rho_0^6)^{3/2} - 3\rho_0 \sqrt{(-1+\rho_0^4)(\rho_0^6-\rho_m^6)} [p_0^2 \rho_0^4 (-2+\rho_0^4) + 6a_2(\rho_0^6-\rho_m^6) - 12(-1+\rho_0^4)(d_4\rho_0^6 + 2b_4\rho_m^6)] \Big], \tag{2.81}$$

and in the above, we are using the compact notation for $p_0' \equiv \partial_{\rho_0} p_0$ based on the chain rule. Since an infinitesimal change in x_0 also varies τ_0, the derivative acts on both arguments of $p_0(\tau_0, x_0)$.

Similarly, the divergent part reads

$$S_{\Sigma(2)}^{\text{div}} = -K^2 \int_\epsilon^{\rho_m} d\rho_0 \frac{p_0^2(-1+2\rho_0^4)\rho_m^3}{6\rho_0(-1+\rho_0^4)^{3/2}(\rho_0^6-\rho_m^6)^{1/2}}, \tag{2.82}$$

with ϵ to regulate the integral. To regularize the divergent term, the following counterterm is added,

$$S_{\Sigma(2)}^{\text{counter}} = \frac{K^2}{6} p_0^2(\tau_*, x_*) \int_\epsilon^{\rho_m} \frac{d\rho_0}{\rho_0}, \tag{2.83}$$

together with a finite contribution to make the regularization scheme independent,

$$S_{\text{cor}} = -\frac{1}{6} K^2 p_0^2(\tau_*, x_*) \log \rho_m. \tag{2.84}$$

Preparing Eq. (2.81)–Eq. (2.84) for numerics with the usual change of variable of $\rho_0 = \rho_m(1-q^2)$, the final expression including all terms,

$$S_{\Sigma(2)} = S_{\Sigma(2)}^{\text{fin}} + S_{\Sigma(2)}^{\text{div}} + S_{\text{counter}} + S_{\text{cor}} + \delta S_{\Sigma(0)}, \tag{2.85}$$

will take the form

---

[10] We assume the branch in the solutions that satisfies $x_m > x_0$.

[11] We have neglected the time derivatives over p_0.

$$\begin{aligned}S_{\Sigma(2)} = {}& K^2 \int_0^1 \frac{qdq}{9\rho_m^8(1-\rho_m^4(-1+q^2)^4)^2(-1+(1-q^2)^6)} \Big[-36\rho_m^{10} f_2(-1+\rho_m^4(-1+q^2)^4)(-1+(1-q^2)^6)(1-q^2)^4 \\ & - 4p_0' p_0 \rho_m^9 (1-\rho_m^4(1-q^2)^4)^{3/2}(1-(1-q^2)^6)^{3/2} - 3\rho_m^4(1-q^2)\sqrt{(-1+(1-q^2)^6)(-1+(1-q^2)^4\rho_m^4)} \\ & \times [p_0^2\rho_m^4(1-q^2)^4(-2+(1-q^2)^4\rho_m^4) + 6a_2\rho_m^6(-1+(1-q^2)^6) - 12\rho_m^6(-1+\rho_m^4(1-q^2)^4)(d_4(1-q^2)^6+2b_4)]\Big] \\ & - K^2 \int_0^1 qdq \frac{p_0^2(-1+2(1-q^2)^4\rho_m^4)}{3(1-q^2)(-1+\rho_m^4(1-q^2)^4)^{3/2}(-1+(1-q^2)^6)^{1/2}} + \frac{K^2}{3} p_0^2(t_*, x_*)\left(\int_0^1 \frac{qdq}{1-q^2} - \frac{1}{2}\log\rho_m + \frac{5}{12}\right),\end{aligned} \tag{2.86}$$

with $p_0' \equiv \partial_{\rho_0} p_0$.

Figures 8(a)–9(f) represent $S_{\Sigma(2)}$, the perturbation to the total EE at $\mathcal{O}(l^2)$, in the $x-\tau$ plane. They are parts of our main results as they have not been reported in any form to the best of our knowledge and perhaps represent the most insightful aspects of EE.

The first thing to notice is the way profiles for EE change when we vary ρ_m. This is apparent by comparing Figs. 6(b)–6(e) in the last section against Figs. 8(a)–8(d). A small dip appears at $\tau \sim 0$ in Figs. 8(a)–8(d) that its magnitude grows as we reduce the value of α. As it is shown in 8(a)–8(d), by gradually increasing values of ρ_m, the maximum of the late-time saturated value for EE reduces. In Figs. 9(a)–9(c), we vary the tuning parameter α from $\frac{1}{2}$ to $\frac{1}{8}$. This causes the dip to get a pinching shape along the τ direction. Similarly, we can change σ, which

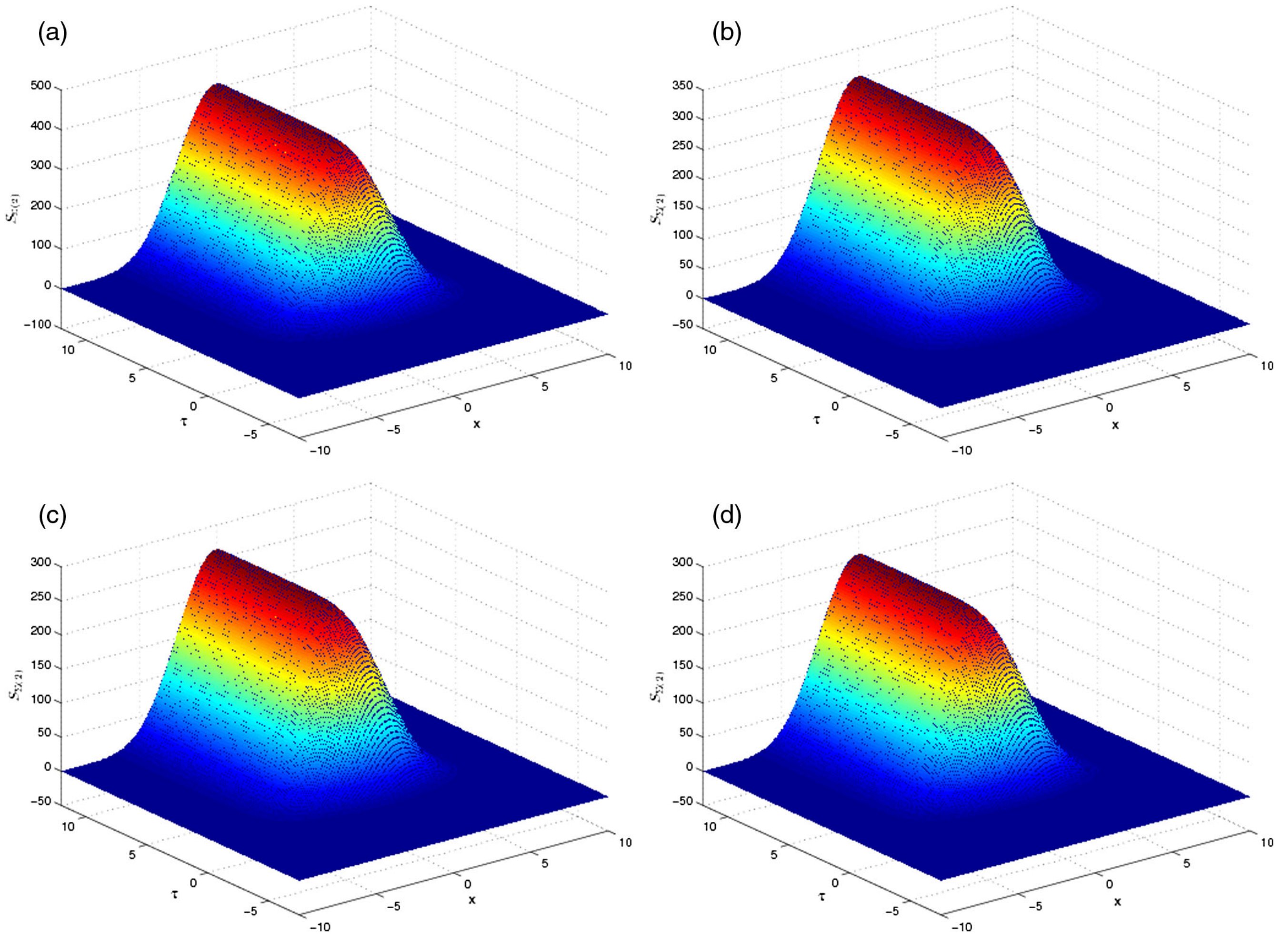

FIG. 8. In the above figures, time evolutions of $S_{\Sigma(2)}$ for case II, are depicted. From (a)–(d), we increase the value of ρ_m to reach the maximum thermalization. Fixed tuning parameters such as $\alpha = 1$ and $\sigma = \sqrt{L_x}$ together with $N_x = N_\rho = 20$ Chebyshev points have been used. The number of time steps for the fourth-order Runge-Kutta has been 7810.

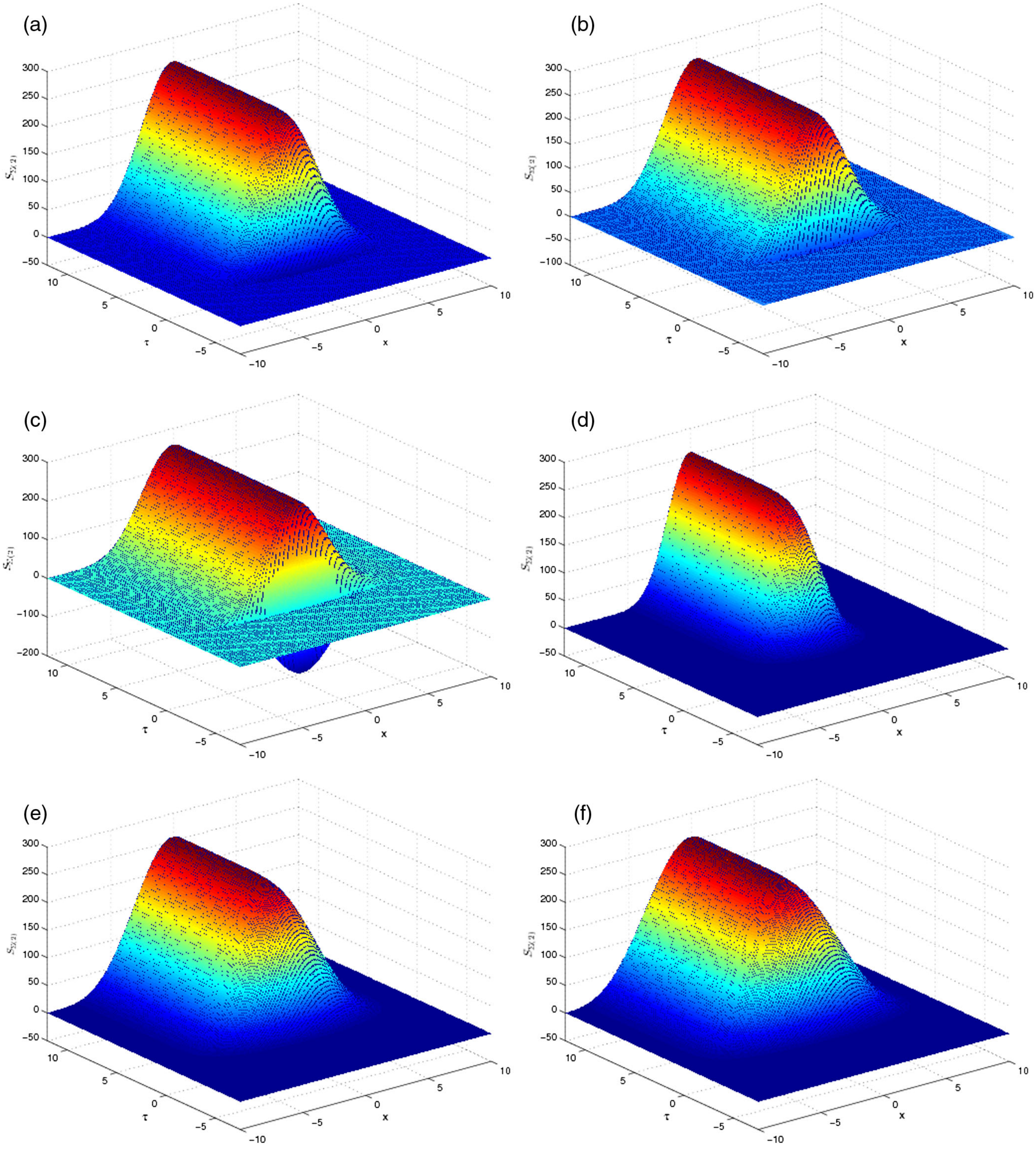

FIG. 9. Plots of the time evolution of the entanglement entropy in case II. In (a)–(c), the value of α has been reduced, while in (d)–(f), we are increasing the tuning parameter σ. The numerical setup is identical to the last figure.

increases the size of the dip sideways along the x axis. These are shown in Figs. 9(d)–9(f).

Comparing these figures with those given in the last section makes it easy to interpret the physics behind EE. In the last section, we found an approximate length for the correlation length. This will allow us to concentrate on the pair of entangled quasiparticles from an arbitrary Cauchy surface within this length. Our system has a strip geometry, and in case I, the boundary is at $[-y_m, y_m]$, and it is extended to infinity in the x direction, whereas in case II, boundaries are at $[-x_m, x_m]$ and are extended to infinity along the y axis. The direction of inhomogeneity is along the x axis in both cases. The EE originates from entangled quasiparticles that have the chance to reach the boundaries of the system. In case I, the quench produces the quasiparticles out of the vacuum, and Figs. 7(a)–7(f) show that pairs that are created at $x = 0$ have the highest chance to reach the boundaries at $[-y_m, y_m]$ assuming they dispatch in opposite directions. Equivalently, as much as they are off the symmetry axis, their chances are lower, and so is their contribution to the EE. Note that what we are plotting are the perturbations of EE at $\mathcal{O}(l^2)$. This situation can be compared with case II, where quasiparticles that are produced at $x = 0$ and want to reach the boundaries at $[-x_m, x_m]$ have to overcome the Gaussian disturbance. This can be put in simple words using Cardy's suggestion [8] to define an entanglement entropy current. In case I, the current induced by the quench is along the axis of the produced quasiparticles. In contrast, the latter current is perpendicular to the path of the quasiparticle pairs in case II and explains the presence of the dip in Figs. 9(a)–9(f).

III. CONCLUSIONS

Throughout this article, we studied various observables such as the apparent horizon, two-point Wightman functions and entanglement entropy to study the physics of thermalization. Our method to derive the system far from equilibrium was the generalization of the setup described by Butchel *et al.* in Ref. [20] for quenches, and we made it inhomogeneous. We then solved the corresponding coupled equations of motion using the spectral method outlined by Chesler and Yaffe [5].

The study of the apparent horizon as a local observable showed the presence of excitations out of the vacuum of $\mathcal{N} = 4$ SYM, created by the mass gap that our quench produces. Different behaviors of these excitations or quasiparticles were observed by varying the quench tuning parameters such as the width of the Gaussian profile, σ, or the time scale of the quench α. It was shown that profiles of the apparent horizon for values of $\alpha \sim 1$ were very similar to profiles of the quench but for $\alpha \sim 0$ a universal behavior was emerging. Increasing σ showed that the mass gap excitations would fill up the available space.

Having an extra nontrivial spatial direction on the boundary allowed us to consider different scenarios that we depicted in Fig. 2. In both cases I and II, the correction to the correlation function at $\mathcal{O}(l^2)$, where l is the order of the backreaction, was considered. Corrections to the Wightman function in case I were symmetric along the $x = 0$ axis unlike case II. The latter had a contribution from one of the components of the metric that was an odd function in x. In both cases, corrections underwent a phase transition that is seen by a change of sign. Since the correlator measures the interference of an infinite number of momentum modes [8], by speculating about our figures, we could parametrize the path of these modes departing from an arbitrary initial time until their interference by $\tau = x/v_{\max}$. Our plots suggest that our quenches belong to the class of $v_{\max} \sim 1$. The study of the correlation functions in both cases I and II also revealed that the physics of thermalization is not diffusive (or at least it is very negligible) as far as we could compare the amplitudes in the two sets of figures.

Similar to the Wightman correlation functions, we used the extra nontrivial spatial direction to study EE in various strip boundary setups. These cases were the extensions of the configurations mentioned in Fig. 2. As we increased the depth in which the minimal surface could probe in the bulk, the EE's evolution followed the profile of the source on the boundary more closely. In case I, the fingerprint of the quasiparticles reaching their horizon could be seen as a slight wiggle on the surface of the EE in the x-τ plane. The setup in case II gives a completely different profile for the EE. This later configuration was an interesting part of our paper due to its novelty and a description in terms of the entanglement current of Cardy *et al.* [8] and could illuminate the underlying physics. We think this result requires further investigation in different setups such as the entangling hemisphere.

As we mentioned above, our study confirmed that the underlying physics of thermalization is not of a diffusive nature at strong couplings, although defining quantities such as currents seem to be inevitable. In fact, physics of thermalization after a quench in many ways is very similar to the physics of far-from-equilibrium isotropization. Consider the two priory different problems, where the first one explains the equilibration of $\mathcal{N} = 4$ SYM in the following holographic setup [5],

$$\begin{aligned} ds^2 = 2d\tau dr - A(\tau, r)d\tau^2 + \Sigma^2(\tau, r)e^{-2B(\tau,r)}dx_L \\ + \Sigma^2(\tau, r)e^{B(\tau,r)}d\mathbf{x}_T, \end{aligned} \tag{3.1}$$

with $r \equiv 1/\rho$ the (inverse) radius of the bulk and where $A(\tau, r)$ and $\Sigma(\tau, r)$ are the warp factors and $B(\tau, r)$ is a function that parametrizes the isotropization with respect to the longitudinal and transverse planes. And the second one is our quench problem with a more simplified background considered in Ref. [20],

$$ds^2 = 2d\tau dr - A(\tau, r)d\tau^2 + \Sigma(\tau, r)^2 d\mathbf{x}^2. \tag{3.2}$$

Upon insertion of Eq. (3.1) and Eq. (3.2) in Einstein equations, the equations of motion will take a specific form [5,20]. We list those of the isotropization problem on the left-hand side and those of the quench on the right-hand side,

$$\begin{gathered} \Sigma\dot{\Sigma}' + 2\Sigma'\dot{\Sigma} - 2\Sigma^2 = 0, \\ \Sigma\dot{\Sigma}' + 2\Sigma'\dot{\Sigma} - 2\Sigma^2 + \frac{1}{12}m^2\phi^2\Sigma^2 = 0, \end{gathered} \tag{3.3}$$

$$\Sigma\dot{B}' + \frac{3}{2}(\Sigma'\dot{B} + B'\dot{\Sigma}) = 0,$$

$$\Sigma\dot{\phi}' + \frac{3}{2}(\Sigma'\dot{\phi} + \phi'\dot{\Sigma}) - \frac{1}{2}\Sigma m^2\phi = 0, \tag{3.4}$$

$$A'' + 3B'\dot{B} - 12\frac{\Sigma'\dot{\Sigma}}{\Sigma^2} + 4 = 0,$$

$$A'' + \phi'\dot{\phi} - 12\frac{\Sigma'\dot{\Sigma}}{\Sigma^2} + 4 - \frac{1}{6}m^2\phi^2 = 0, \tag{3.5}$$

$$\ddot{\Sigma} + \frac{1}{2}(\dot{B}^2\Sigma - A'\dot{\Sigma}) = 0,$$

$$\ddot{\Sigma} + \frac{1}{2}\left(\frac{\dot{\phi}^2\Sigma}{3} - A'\dot{\Sigma}\right) = 0, \tag{3.6}$$

$$\Sigma'' + \frac{1}{2}(B')^2\Sigma = 0, \qquad \Sigma'' + \frac{1}{6}(\phi')^2\Sigma = 0. \tag{3.7}$$

In the above, we used $h' \equiv \partial_r h$ and $\dot{h} \equiv \partial_\tau h + \frac{1}{2}\partial_r h$. To make a connection between the two lists of equations on the right- and left-hand sides, we realize that by choosing a symmetry factor $B \equiv \frac{\phi}{\sqrt{3}}$, apart from extra mass terms,[12] the two sets of coupled differential equations are identical.

IV. FUTURE DIRECTION

Another important aspect of the study of the quantum quenches is their universal scaling behavior [25,26]. It has been shown that for relatively fast quenches, the expectation value of the boundary operator scales according to its original source. Explicitly, this means that from the expansion of the scalar field in the Eddington-Finkelstein frame

$$\phi(\tau,\rho) = \rho p_0(\tau) + \rho^2\partial_\tau p_0 + \rho^3 p_2(\tau) + \mathcal{O}(\rho^2 \ln\rho), \tag{3.8}$$

if the coupling in Eq. (1.1) behaves according to $\lambda = \lambda_0(\frac{\tau}{\delta\tau})^\kappa$, the normalizable part of the scalar field in Eq. (3.8) will turn out to be [25,26]

$$p_2(\tau) \sim \delta\tau^{-2}\left(\frac{\tau}{\delta\tau}\right)^{\kappa-2}, \tag{3.9}$$

with $\delta\tau$ being the characteristic time that is relevant for the problem. To find Eq. (3.9), the limit of $\delta\tau \to 0$ has been taken, and information regarding the four-dimensional fermionic operator with $\Delta = 3$ has been used. Furthermore, the origin of this behavior is a direct consequence of the causality. Along the same line, we can ask if the above universality is preserved or not analytically in the inhomogeneous case.

An easy way to partially answer the above question is the following: for fast quenches, nonlinearities and higher-order backreactions can be neglected since in a short time perturbations cannot propagate through the whole bulk space [25]. Therefore, one expects that an intuitive answer in the neighborhood of the boundary should work. Neglecting logarithmic corrections and higher-order terms for simplicity, the boundary terms could be written as

$$\phi = l(\rho p_0 + \rho^2\partial_\tau p_0 + \rho^3 p_2), \tag{3.10}$$

$$A = \frac{1}{\rho^2} - \rho^2 + l^2\left(-\frac{1}{6}p_0^2 + \rho^2 a_2\right), \tag{3.11}$$

$$\Sigma_d = \frac{1}{\rho} + l^2\left(-\rho^2\frac{p_0^2}{12} - \rho^3\frac{p_0\partial_\tau p_0}{9} + \rho^4 d_4\right), \tag{3.12}$$

$$\Sigma_b = \frac{1}{\rho} + l^2\left(-\rho^2\frac{p_0^2}{12} - \rho^3\frac{p_0\partial_\tau p_0}{9} + \rho^4 b_4\right), \tag{3.13}$$

$$\Xi = l^2\left(-\rho\frac{p_0\partial_x p_0}{9} + \rho^2 f_2\right), \tag{3.14}$$

where in the above p_0, p_2, a_2, b_4, d_4 and f_2 depend on (τ, x). An identical argument that was mentioned to reproduce Eq. (3.9) still implies to Eq. (3.10). This is due to the absence of any spacial derivative in the right-hand side at that specific order. While the scaling behaviors in Eq. (3.11), Eq. (3.12) and Eq. (3.13) are suppressed, a new feature appears in the field Ξ. But $\Xi \ll 1$, so its backreaction on the other components implies that the universality breaks in a very naive way. A more convincing answer to the above question requires an analytic derivation.

ACKNOWLEDGMENTS

The author is indebted to the organizers of the workshop on "Numerical Holography" at CERN, December 2014, especially, Larry Yaffe and Michal Heller. The author is grateful to have had stimulating discussions with Matthias Blau, Konstantinos Siampos, and Dimitrios Giataganas. The author also acknowledges discussions, in the early stages on the subject, with Mohamad Aliakbari and Hajar Ebrahim. The author gratefully acknowledges the referee's feedback that boosted the quality of the paper. This work was supported by the Swiss National Science Foundation (SNF) under Grant No. 200020-155935 and Natural Sciences and Engineering Council of Canada.

APPENDIX: DERIVATIONS AND NUMERICAL IMPLEMENTATIONS

1. Setup

As mentioned before, the problem at hand is a scalar field on an AdS-black brane spacetime. Starting with the

---

[12] Although the mass terms played a key role in our quenches, we could argue that we start our simulation from a rather nontrivial initial data and then study the evolution without turning on any quenches.

following ansatz for the metric in an infalling observer's picture (Eddington-Finkelstein coordinates), it reads

$$ds_5^2 = -A(\tau, r, x)d\tau^2 + \Sigma_d(\tau, r, x)^2 dx^2 + \Sigma_b(\tau, r, x)^2 d\vec{y}^{\,2} + 2\Xi(\tau, r, x)d\tau dx + 2drd\tau. \tag{A1}$$

Our five-dimensional Einstein-Hilbert action with a negative cosmological constant is given by

$$S_5 = \frac{1}{16\pi G_5}\int d^5x\sqrt{-g}\left(R + 12 - \frac{1}{2}(\partial\phi)^2 - \frac{1}{2}m^2\phi^2 + \mathcal{O}(\phi^3)\right), \tag{A2}$$

where we have neglected higher-order interactions. We may also use the inverse of the bulk radius defined by $\rho = 1/r$, and x is the special direction that we apply the inhomogeneity. As a wave packet $\phi(\tau, \rho, x)$ is prepared on the boundary, it will evolve according to the equations of motion, and all other fields will be affected by the inhomogeneity. In the following, we will suppress such a functionality, (τ, r, x), to simplify the notation.

Here is how the setup works. The scalar field is zero at the beginning as we turn on the quench at $\tau = -\infty$. At a region around $\tau = 0$, the mass coupling of the fermionic operator with $m^2 = -3$ is switched on, and this change in the boundary conditions alters the profiles of the fields in the dual bulk space. Classical excitations of the scalar field collapsing into the black hole will backreact on the metric. Eventually, at the asymptotic future, all the bulk fields will have a new equilibrium, thermalized or partially thermalized configurations. If the final configuration is static and globally thermalized, the black hole has a new temperature and correspondingly a new size consistent with the initial data at the asymptotic past and the boundary conditions.

We focus on $m^2 = -3$; the scalar field is then mapped to a dual fermionic mass operator $\Delta = 3$ in a mass-deformed and thermal $\mathcal{N} = 2^*$ gauge theory in $d = 4$ flat spacetime. As argued in Ref. [20], high temperature quenches $m/T \ll 1$ are dual to the perturbative scalar field in the background geometry. At the leading order, the static nonequilibrium equation for ϕ is given by

$$\frac{m^2}{\rho^2}\phi_{\text{equil}} - \partial_x^2\phi_{\text{equil}} + \frac{1}{\rho}(3 + \rho^4)\partial_\rho\phi_{\text{equil}} - (1 - \rho^4)\partial_\rho^2\phi_{\text{equil}} = 0. \tag{A3}$$

The solution to the above equation is the profile for the scalar field that corresponds to the equilibrium configuration at the asymptotic future. Unless $\partial_x\phi_{\text{equil}} = 0$, there is no analytic solution in terms of the hyperbolic functions [20] for Eq. (A3),

$$\phi_{\text{equil}}(\rho) = l\pi^{-1/2}\Gamma\left(\frac{3}{4}\right)^2 {}_2F_1\left(\frac{3}{4}, \frac{3}{4}, 1, 1 - \rho^4\right)\rho^3, \tag{A4}$$

and information about the final general profile will be available through numerics or through approximations in extreme regimes [31]. For further applications of Eq. (A1), refer to Ref. [32] where they study the physics of anisotropy.

2. Backreaction

A simple study of the equations of motion shows that if the fluctuations of the scalar field are at the scale of l, then the effect from backreaction appears at l^2. Therefore, for simplicity, we consider an expansion of the form

$$\phi(\tau, \rho, x) = l\hat{\phi}(\tau, \rho, x) + \mathcal{O}(l^3), \tag{A5}$$

$$A(\tau, \rho, x) = \frac{1}{\rho^2} - \rho^2 + l^2\hat{A}(\tau, \rho, x) + \mathcal{O}(l^4), \tag{A6}$$

$$\Sigma(\tau, \rho, x) = \frac{1}{\rho}e^{l^2\hat{\Sigma}(\tau,\rho,x)} + \mathcal{O}(l^4), \tag{A7}$$

$$\Xi(\tau, \rho, x) = l^2\hat{\Xi} + \mathcal{O}(l^3) \tag{A8}$$

in the above; we mean $\Sigma \in \{\Sigma_d, \Sigma_b\}$.

We can classify the equations into two categories: evolution equations and constraints. Given some initial state or profile for the field, constraints allow us to extract the value of the dependent fields on the former initial profiles throughout the domain of the computation. On the other hand, evolution equations permit the evolution of the initial state into later times. According to this distinction, the following constraints and evolution equations are obtained. The Klein-Gordon equation of motion for the scalar field that gives the evolution of the scalar field is given by

$$\frac{m^2}{\rho^2}\phi - \partial_x^2\phi + 3\frac{\partial_\rho\phi}{\rho} + \rho^3\partial_\rho\phi - \partial_\rho^2\phi + \rho^4\partial_\rho^2\phi - 3\frac{\partial_\tau\phi}{\rho} + 2\partial_\tau\partial_\rho\phi = 0. \tag{A9}$$

Then, the constraint for the combination of $\Sigma_d + 2\Sigma_b$ will be

$$\partial_\rho^2(\Sigma_d + 2\Sigma_b) + \frac{1}{2}(\partial_\rho\phi)^2 = 0; \tag{A10}$$

knowing the profiles for Σ_b and ϕ allows us to find Ξ by the constraint

$$\partial_\rho^2\Xi - 4\frac{\Xi}{\rho^2} + \frac{\partial_\rho\Xi}{\rho} + \frac{\partial_x\phi\partial_\rho\phi}{\rho^2} + 4\frac{\partial_\rho\partial_x\Sigma_b}{\rho^2} = 0. \tag{A11}$$

A similar description also holds for determining the value of the warp factor A in the whole domain of the computation,

$$\partial_\rho^2 A + \frac{m^2\phi^2}{3\rho^4} - \frac{\partial_\rho A}{\rho} - \frac{2}{\rho^3}\partial_\rho[\Sigma_d + 2\Sigma_b] - 2\rho\partial_\rho[\Sigma_d + 2\Sigma_b] + \partial_\rho\partial_x\Xi + \frac{2}{\rho^3}\partial_\tau[\Sigma_d + 2\Sigma_b] - \frac{\partial_\rho\phi\partial_t\phi}{\rho^2} - \frac{2}{\rho^2}\partial_\tau\partial_\rho[\Sigma_d + 2\Sigma_b] = 0. \tag{A12}$$

After determining the initial profiles for all the fields according to the above constraints, the set of coupled evolution equations for Σ_d and Σ_b,

$$-2A - \frac{m^2}{6}\frac{\phi^2}{\rho^2} + \rho\Xi + \rho^5\partial_x\Xi - \partial_x^2\Sigma_b + \rho\partial_\rho A + \frac{\partial_\rho\Sigma_d}{\rho} - \rho^3\partial_\rho\Sigma_d + 5\frac{\partial_\rho\Sigma_b}{\rho} - \rho^3\partial_\rho\Sigma_b - \partial_\rho^2\Sigma_b + \rho^4\partial_\rho^2\Sigma_b - \frac{\partial_\tau\Sigma_d}{\rho} - 5\frac{\partial_\tau\Sigma_b}{\rho} + 2\partial_\tau\partial_\rho\Sigma_b = 0, \tag{A13}$$

together with

$$\frac{m^2}{6}\frac{\phi^2}{\rho^2} - \frac{m^2}{6}\rho^2\phi^2 - \rho(1+\rho^4)\partial_x\Xi + \frac{\rho^2}{2}\partial_x^2 A - \frac{\rho}{2}(1-\rho^4)\partial_\rho A - \frac{1}{\rho}\partial_\rho[\Sigma_d + 2\Sigma_b] + \rho^7\partial_\rho[\Sigma_d + 2\Sigma_b] + \frac{\rho^2}{2}(1-\rho^4)\partial_\rho^2 A - \frac{3}{2}\rho\partial_t A + \left(\frac{1}{\rho} + \rho^3\right)\partial_\tau\Sigma_d + 2\left(\frac{1}{\rho} + \rho^3\right)\partial_\tau\Sigma_b - \frac{1}{2}(\partial_\tau\phi)^2 + \rho^2\partial_\tau\partial_x\Xi - \partial_\tau^2[\Sigma_d + 2\Sigma_b] = 0, \tag{A14}$$

permits solving for future profiles of the fields. Finally, the constraint and evolution equation for Ξ are given by

$$2A + \frac{m^2}{6}\frac{\phi^2}{\rho^2} - 2\rho\partial_x\Xi + 2\rho(1+\rho^4)\partial_x\Xi + \frac{1}{2}(\partial_x\phi)^2 + 2\partial_x^2\Sigma_b - \rho\partial_\rho A - \frac{2}{\rho}\partial_\rho[2\Sigma_d + \Sigma_b] + 2\rho^3\partial_\rho\Sigma_b + \rho^2\partial_\rho\partial_x\Xi + \partial_\rho^2\Sigma_d - \rho^4\partial_\rho^2\Sigma_d + \frac{2}{\rho}\partial_\tau[2\Sigma_d + \Sigma_b] - \partial_\tau\partial_\rho\Sigma_d = 0, \tag{A15}$$

to be solved with

$$-4\frac{\Xi}{\rho^2} + 4\rho^2\Xi + \frac{\partial_x A}{\rho} + \frac{\partial_\rho\Xi}{\rho} - \rho^3\partial_\rho\Xi - \partial_\rho\partial_x A + (1-\rho^4)\partial_\rho^2\Xi - 2\frac{\partial_\tau\Xi}{\rho} + \frac{\partial_x\phi\partial_t\phi}{\rho^2} + 4\frac{\partial_\tau\partial_x\Sigma_b}{\rho^2} - \partial_\tau\partial_\rho\Xi = 0. \tag{A16}$$

Focusing on the fermionic operator as discussed in Ref. [19], throughout our computation, we will assume $m^2 = \Delta(\Delta - d) = -3$, where Δ is the conformal dimension of the scalar field $\phi(\tau, \rho, x)$. Now that we have both the constraints and the evolution equations, it is important to find the boundary expansion on the AdS$_5$ that follows from the Einstein equations by successive iteration of the solutions. The few interesting terms of the expansion of each field are listed and will be used extensively throughout the paper,[13]

$$\hat{\phi} = \rho p_0 + \rho^2\partial_\tau p_0 + \rho^3\left[p_2 - \frac{1}{2}\ln\rho(\partial_x^2 p_0 - \partial_\tau^2 p_0)\right] + \rho^4\left(\partial_\tau p_2 - \frac{1}{3}\partial_\tau^3 p_0\right) - \frac{\rho^4\ln\rho}{2}(\partial_\tau\partial_x^2 p_0 - \partial_\tau^3 p_0) + \mathcal{O}(\rho^5), \tag{A17}$$

$$\hat{A} = -\frac{1}{6}p_0^2 + \rho^2\left(a_2 + \frac{\ln\rho}{18}[(\partial_x p_0)^2 + 3(\partial_\tau p_0)^2 + p_0(\partial_x^2 p_0 - 3\partial_\tau^2 p_0)]\right) + \mathcal{O}(\rho^3), \tag{A18}$$

$$\hat{\Sigma}_d = -\frac{1}{12}\rho^2 p_0^2 - \frac{1}{9}\rho^3 p_0\partial_\tau p_0 + \rho^4\left(d_4 + \frac{\ln\rho}{72}[-4(\partial_x p_0)^2 + p_0(5\partial_x^2 p_0 - 3\partial_\tau^2 p_0)]\right) + \mathcal{O}(\rho^5), \tag{A19}$$

$$\hat{\Sigma}_b = -\frac{1}{12}\rho^2 p_0^2 - \frac{1}{9}\rho^3 p_0\partial_\tau p_0 + \rho^4\left(b_4 + \frac{\ln\rho}{72}[2(\partial_x p_0)^2 + p_0(2\partial_x^2 p_0 - 3\partial_\tau^2 p_0)]\right) + \mathcal{O}(\rho^5), \tag{A20}$$

$$\hat{\Xi} = -\frac{1}{9}\rho p_0\partial_x p_0 + \rho^2\left(f_2 + \frac{\ln\rho}{12}[p_0\partial_\tau\partial_x p_0 - 2\partial_x p_0\partial_\tau p_0]\right) + \mathcal{O}(\rho^3). \tag{A21}$$

Note that in practice, we have worked out the above expansion to $\mathcal{O}(\rho^8)$. Further, we should draw the attention of the reader to the normalizable terms such as $\{p_2, a_2, f_2, d_4, b_4\}$. These coefficients are the response of the fields to the alterations in the system.

3. 2D Chebyshev lattice

General overview.—In what follows, we do the computations as symbolically as possible. Our goal here has been to achieve relatively very small rounding errors through successive operations that have been carried out. The fact

---

[13] Similar to Ref. [20], we make an implicit gauge choice in writing the following boundary expansions since metric components are invariant under residual diffeomorphism.

that smooth functions can be approximated in a creative way by polynomial interpolation in Chebyshev points and the use of fast Fourier transform allow us to use a new sort of polynomials called Chebyshev polynomials. To do the numerics in a stable and effective way, accuracy to within roughly machine precision can be achieved using spectral methods.

In the interval of $0 < \rho < 1$, a convenient basis of expansion in terms of the Chebyshev polynomials $T_n(z) \equiv \cos(n \cos^{-1} z)$ will have the form

$$g(\rho) = \sum_{n=0}^{M} \alpha_n T_n(2\rho - 1), \tag{A22}$$

which is nothing other than rewriting the Fourier expansion with a change of variable $\theta \equiv \cos^{-1}(2\rho - 1)$. In a general approach, pseudospectral or collocation method, one finds the expansion coefficients α_n by inserting the above truncated series into the differential equation of interest and turn the problem into an eigenvalue problem. We should point out that, although in the conventional Fourier transformation one is interested in equally spaced lattices, in the spectral method, we avoid this primitive setup and instead use basis function that are matched by the position of the maximums/minimums and end points of the Mth Chebyshev basis. In our case, for the interval [0, 1], these are given by

$$\rho_m = \frac{1}{2}\left(1 - \cos\frac{m\pi}{M}\right); \tag{A23}$$

with the knowledge of α_n, we reconstruct the whole function $\{g_m \equiv g(\rho_m)\}$ from the collocation grid points.

The range $x \in [0, 1]$ is the most convenient one to use, but sometimes the other option, $z \in [-1, 1]$, is required. The map between the two sets is given by $x = \frac{1}{2}(1 + z)$, and this leads to a shifted[14] Chebyshev polynomial [33]

$$T_n^*(x) = T_n(z) = T_n(2x - 1). \tag{A24}$$

We will use this latter set for the spectral grid in the x direction where we need the boundary in the range $[-L_x, L_x]$.

The concept of Chebyshev points can be extended to differential operators and we will be working with Chebyshev differential matrices later on. Meanwhile, there are various interesting identities [34] for the Chebyshev polynomials that will be useful throughout this Appendix. They satisfy

$$\sqrt{1-x^2}\,\frac{d}{dx}(\sqrt{1-x^2}) + n^2 T_n(x) = 0, \tag{A25}$$

and their explicit integral evaluates to

$$\int_{-1}^{1} dx T_n(x) = -\frac{2}{n^2 - 1} \text{for even } n, \tag{A26}$$

while the value of the integral is zero for any odd n. At the boundaries, they satisfy

$$T_n(x = \pm 1) = (\pm 1)^n, \qquad \frac{dT_n}{dx}\bigg|_{x=\pm 1} = (\pm 1)^{n+1} n^2,$$
$$\frac{d^2 T_n}{dx^2}\bigg|_{x=\pm 1} = \frac{1}{3}(\pm 1)^n (n-1) n^2 (n+1). \tag{A27}$$

2D aspects.—The above one-dimensional boundary value problem can be extended to higher dimensions. To be specific, here, we use a 2D setup. For such a problem, we naturally set up a grid based on Chebyshev points in each direction independently. This is usually called a *tensor product grid*. It is interesting to note that, in comparison with an equally spaced grid, the Chebyshev grid is $2/\pi$ times as dense in the middle, and in our current 2D setup, this ratio becomes $(2/\pi)^2$. Thus, the majority of the grid points lies near the boundaries. As the enforcing boundary condition is applied at $\rho = 0$, this will enhance the resolution. Therefore, the tensor product construction of a spectral grid is the natural way to go. This can easily be done by the tensor product in linear algebra; for instance, for two matrices A and B, the *Kronecker product* is given by $A \otimes B$. That is, if A and B are matrices of dimensions $p \times q$ and $r \times s$ respectively, then $A \otimes B$ is a matrix of dimension $pr \times qs$ with $p \times q$ block forms, where each i and j block has the value of $a_{ij}B$.

With a data set represented symbolically as $(v_1, v_2, \ldots, v_{10})^T$, we can use the one-dimensional (1D) representation of the differential operators to find a representation of its counterpart in two dimensions in the following way:

$$L_{N_\rho \times N_x} = I_{N_\rho} \otimes D_{N_x} + D_{N_\rho} \otimes I_{N_x}. \tag{A28}$$

Using the above representation, it is also possible to derive D_N^2 of the Laplace operator on the above lattices. In principle, we could have used the polar coordinates, but we stick to the choice of the Cartesian one since we are imposing the boundary condition exactly at $\rho = 0$, and we cannot avoid any creative trick to avoid this point. One extra complication with respect to the 1D setup is the issue of corner compatibility, which states that

$$\alpha_\pm(x = L_{\max}) = \beta_+(\rho = 0 \quad \text{and} \quad 1),$$
$$\alpha_\pm(x = -L_{\max}) = \beta_-(\rho = 0 \quad \text{and} \quad 1). \tag{A29}$$

In the above, we assume that the boundary values for $\rho = 0$ and $\rho = 1$ are given by $\alpha_+(x)$ and $\alpha_-(x)$ respectively and

---

[14] The map for the general case of $x \in [a, b]$ can be constructed similarly using $s = \frac{2x-(a+b)}{b-a}$ for $x \in [-1, 1]$.

the corresponding boundary values on vertical walls at $x = \pm L_{\max}$ are equal to $\beta_{\pm}(\rho)$. The effect of these corner conditions becomes prominent when we calculate derivatives of the fields.

After discretizing the problem in rectangular Cartesian coordinates, we use the generalization of the pseudospectral method in two dimensions. For instance, a function, $f(\rho, x)$, has an expansion as linear combinations of Chebyshev polynomials,

$$f^{N,L}(\rho, x) = \sum_{l=0}^{L} \sum_{n=0}^{N} \hat{\rho}_{ln} T_n(\rho) T_l(x); \tag{A30}$$

here, the $\hat{\rho}_{ln}$s are the 2D spectra of $f(\rho, x)$. In addition, N and L are the number of collocation points in ρ and x coordinates. In vectorial notation, we rewrite the Chebyshev polynomials in x and ρ directions:

$$\begin{aligned} (\mathbf{T}_x)_{l\lambda} &= (-1)^{\lambda} \cos\left(l\lambda \frac{\pi}{L}\right), \\ (\mathbf{T}_\rho)_{n\nu} &= (-1)^{\nu} \cos\left(n\nu \frac{\pi}{N}\right). \end{aligned} \tag{A31}$$

Based on Fig. 10, the representation for the general solution can then be selected as

$$\begin{aligned} F = (&\underbrace{f_{00}, f_{10}, \ldots, f_{L0}}, \underbrace{f_{01}, f_{11}, \ldots, f_{L1}}, \underbrace{\cdots}, \underbrace{\cdots}, \\ &\underbrace{f_{0N}, f_{1N}, \ldots, f_{LN}})^T. \end{aligned} \tag{A32}$$

These are $(N+1)$ blocks of $(L+1)$ quantities, and each block corresponds to a position in the ρ coordinates.

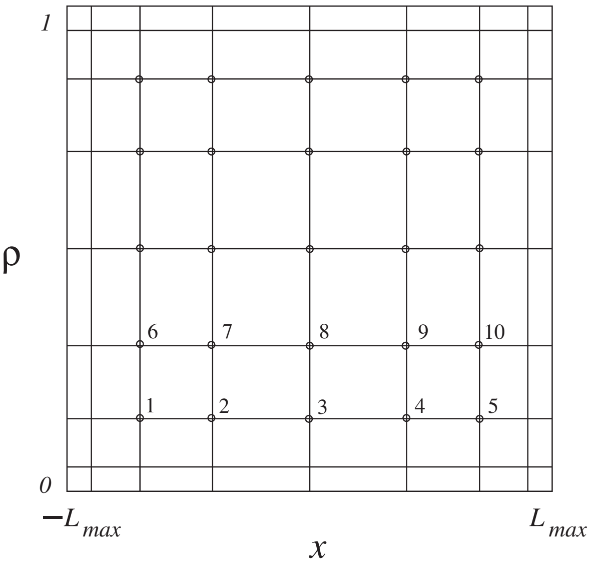

FIG. 10. A tensor product grid; there are two spacial directions. x is the direction of the inhomogeneity, and ρ is the bulk radius. The numbers at each site represent the lexicographic representation of the grid points while doing the operation as a tensor grid.

In this representation, Eq. (A30) will take the compact form of

$$F = (\mathbf{T}_\rho \otimes \mathbf{T}_x) \hat{F}, \tag{A33}$$

which is suitable for our notation throughout the rest of this Appendix.

4. Coupled equations

Our first step in the numerical code is to make the following definitions,

$$\pi(\tau, \rho, x) = \partial_\tau \hat{\phi}(\tau, \rho, x) + \frac{\rho^4 - 1}{2} \partial_\rho \hat{\phi}(\tau, \rho, x), \tag{A34}$$

$$\beta(\tau, \rho, x) = \partial_\tau \hat{\Sigma}_d(\tau, \rho, x) + \frac{\rho^4 - 1}{2} \partial_\rho \hat{\Sigma}_d(\tau, \rho, x), \tag{A35}$$

$$\gamma(\tau, \rho, x) = \partial_\tau \hat{\Sigma}_b(\tau, \rho, x) + \frac{\rho^4 - 1}{2} \partial_\rho \hat{\Sigma}_b(\tau, \rho, x), \tag{A36}$$

$$\chi(\tau, \rho, x) = \partial_\tau \hat{\Xi}(\tau, \rho, x) + \frac{\rho^4 - 1}{2} \partial_\rho \hat{\Xi}(\tau, \rho, x), \tag{A37}$$

that transform Eq. (A9)–Eq. (A15) into more compact forms,

$$\partial_\rho \pi - \frac{3}{2} \frac{\pi}{\rho} = -J_\phi, \tag{A38}$$

$$\partial_\rho^2 (\Sigma_d + 2\Sigma_b) + \frac{1}{2} (\partial_\rho \phi)^2 = 0, \tag{A39}$$

$$\partial_\rho^2 \Xi - 4 \frac{\Xi}{\rho^2} + \frac{\partial_\rho \Xi}{\rho} + \frac{\partial_x \phi \partial_\rho \phi}{\rho^2} + 4 \frac{\partial_\rho \partial_x \Sigma_b}{\rho^2} = 0, \tag{A40}$$

$$\partial_\rho \beta - \frac{1}{\rho} [2\beta + \gamma] = -J_{\Sigma_d}, \tag{A41}$$

$$\partial_\rho \gamma - \frac{1}{2\rho} [\beta + 5\gamma] = -J_{\Sigma_b}, \tag{A42}$$

$$\partial_\rho^2 A - \frac{\partial_\rho A}{\rho} + \frac{-2}{\rho^2} \partial_\rho [\beta + 2\gamma] + \frac{2}{\rho^3} [\beta + 2\gamma] - \pi \frac{\partial_\rho \phi}{\rho^2} = -J_a, \tag{A43}$$

$$\partial_\rho \chi + 2 \frac{\chi}{\rho} - 4 \frac{\partial_x \gamma}{\rho^2} - \pi \frac{\partial_x \phi}{\rho^2} + 2\rho^2 \left(1 - \frac{1}{\rho^4}\right) \partial_\rho \partial_x \Sigma_b = -J_\Xi, \tag{A44}$$

with the sources on the right-hand sides of the above equations defined according to

$$J_\phi = \frac{m^2}{2} \frac{\phi}{\rho^2} - \frac{1}{2} \partial_x^2 \phi - \frac{3}{4} \rho^3 \left(1 - \frac{1}{\rho^4}\right) \partial_\rho \phi, \tag{A45}$$

$$J_{\Sigma_d} = -A - \frac{m^2}{12}\frac{\phi^2}{\rho^2} + \rho\partial_x\Xi - \frac{1}{4}(\partial_x\phi)^2 - \partial_x^2\Sigma_b + \frac{1}{2}\rho\partial_\rho A - \frac{\rho^3}{2}\left(1-\frac{1}{\rho^4}\right)\partial_\rho[2\Sigma_d+\Sigma_b] - \frac{1}{2}\rho^2\partial_\rho\partial_x\Xi, \tag{A46}$$

$$J_{\Sigma_b} = -A - \frac{m^2}{12}\frac{\phi^2}{\rho^2} + \frac{1}{2}\rho\partial_x\Xi - \frac{1}{2}\partial_x^2\Sigma_b + \frac{1}{2}\rho\partial_\rho A - \frac{\rho^3}{4}\left(1-\frac{1}{\rho^4}\right)\partial_\rho[\Sigma_d+5\Sigma_b], \tag{A47}$$

$$J_a = \frac{m^2}{3}\frac{\phi^2}{\rho^4} + \rho\left(1-\frac{1}{\rho^4}\right)\partial_\rho[\Sigma_d+2\Sigma_b] + \frac{\rho^2}{2}\left(1-\frac{1}{\rho^4}\right)(\partial_\rho\phi)^2 + \partial_\rho\partial_x\Xi + \rho^2\left(1-\frac{1}{\rho^4}\right)\partial_\rho^2[\Sigma_d+2\Sigma_b], \tag{A48}$$

$$J_\Xi = -4\rho^2\left(1-\frac{1}{\rho^4}\right)\Xi - \frac{\partial_x A}{\rho} - 2\rho^3\partial_\rho\Xi + \frac{\rho^2}{2}\left(1-\frac{1}{\rho^4}\right)\partial_x\phi\partial_\rho\phi + \partial_\rho\partial_x A - \frac{1}{2}(1-\rho^4)\partial_\rho^2\Xi. \tag{A49}$$

We point out a few comments about the above equations. They are listed chronologically; that is, we start by solving the coupled differential equations starting from Eq. (A38) and ending in Eq. (A44). The equation of motion for the scalar field is not coupled to the other metric components. This is due to the choice of cutoff that we have imposed on the backreaction. From the boundary expansion, it is clear that the x dependence of Σ s does not factorize. Therefore, x dependence of ϕ must not factorize according to Eq. (A39). As is clear from Eq. (A39), knowing the value of the scalar field ϕ_0, everywhere in the bulk, only gives information about the combination of $\Sigma_d+2\Sigma_b$. Moreover, the x dependency of $\Sigma_d+2\Sigma_b$ will be trivial since the derivatives act on the ρ direction.

Extra identities.—In addition to the above differential equations, in this subsection, we derive identities that are useful when we are applying the boundary conditions on the fields.

Summation of Eq. (A41) and Eq. (A42) gives $\beta+2\gamma$ as a function of $\Sigma_d+2\Sigma_b$, that is

$$\partial_\rho[\beta+2\gamma] - \frac{3}{\rho}[\beta+2\gamma] = -J_{\Sigma_d+2\Sigma_b}, \tag{A50}$$

with $J_{\Sigma_d+2\Sigma_b}$ that reads

$$J_{\Sigma_d+2\Sigma_b} = -3A - \frac{m^2}{4}\frac{\phi^2}{\rho^2} + 2\rho\partial_x\Xi - \frac{1}{4}(\partial_x\phi)^2 - 2\partial_x^2\Sigma_b + \frac{3}{2}\rho\partial_\rho A - \frac{3\rho^3}{2}\left(1-\frac{1}{\rho^4}\right)\partial_\rho[\Sigma_d+2\Sigma_b] - \frac{1}{2}\rho^2\partial_\rho\partial_x\Xi, \tag{A51}$$

but the presence of $\partial_x^2\Sigma_b$ requires some extra knowledge of Σ_b. Furthermore, from Eq. (A40), we can solve for $\partial_\rho\partial_x\Sigma_b$ and insert it in Eq. (A44) to obtain

$$\partial_\rho\chi + 2\frac{\chi}{\rho} - 4\frac{\partial_x\gamma}{\rho^2} - \pi\frac{\partial_x\phi}{\rho^2} = -J_{\chi_b}, \tag{A52}$$

with

$$J_{\chi_b} = -2\rho^2\left(1-\frac{1}{\rho^4}\right)\Xi - \frac{5}{2}\rho^3\partial_\rho\Xi + \frac{1}{2\rho}\partial_\rho\Xi - \frac{\partial_x A}{\rho} + \partial_\rho\partial_x A, \tag{A53}$$

and again in the above, extra knowledge of $\partial_x\gamma$ will be necessary to solve for χ.

In addition to the above constraints, we also have

$$d_4 + 2b_4 + \frac{1}{4}p_0p_2 + \frac{1}{32}p_0\partial_x^2p_0 + \frac{1}{6}(\partial_\tau p_0)^2 - \frac{1}{32}p_0\partial_\tau^2p_0 = 0, \tag{A54}$$

and

$$2\partial_x f_2 - \frac{1}{2}p_2\partial_\tau p_0 + \frac{5}{18}\partial_x^2p_0\partial_\tau p_0 + \frac{3}{2}\partial_\tau a_2 + \frac{1}{2}p_0\partial_\tau p_2 + \frac{13}{72}\partial_x p_0\partial_\tau\partial_x p_0 + \frac{11}{72}p_0\partial_\tau\partial_x^2p_0 + \frac{1}{12}\partial_\tau p_0\partial_\tau^2p_0 - \frac{1}{3}p_0\partial_\tau^3p_0 = 0, \tag{A55}$$

which means that in order to extract the evolution of $a_2(\tau,x)$, the coefficient in the warp factor, we have to provide $\partial_x f_2$ in addition to the initial condition of $a_2(\tau_0,x)$. In the rest of this Appendix, we will solve Eq. (A38)–Eq. (A44) and the above identities numerically.

5. Numerical implementation

As we mentioned before, in practice, we have a finite number of points available in the inhomogeneous direction. The cutoff should be chosen with respect to the value of the other parameters such as the size of the system or the profile of the source under consideration. We consider rather a general profile for the source [20,31],

$$p_0(\tau,x)=\frac{1}{2}\left[1+\tanh\left(\frac{\tau}{\alpha}\right)\right]e^{-\frac{x^2}{\sigma^2}}, \tag{A56}$$

and choose the cutoff for the coordinate $x\in[-L_x,L_x]$ with $L_x=10$ and multiple values for $\sigma\in[\sqrt{L_x},\sqrt{1.5L_x}]$ and $\alpha\in[\frac{1}{8},1]$. Each of these parameters simulates a different physical scenario. Parameter α is the scale of the time variation of the quench, unlike σ which is the spacial scale of the inhomogeneity applied to the system. The shape of p_0 has been chosen so that at the asymptotic past the source is zero. In principle, for doing the numerical analysis, we considered the time interval $\tau\in[\tau_i,\tau_f]$ with $\tau_i=-7.5$ and $\tau_f=12$, that works out for our goal similar to Ref. [20].

As it was pointed out in Sec. A 2, near the boundary, we encounter logarithmic divergences that cause numerical instabilities; to tackle them on the lattice, the standard method is to isolate the finite contributions. Therefore, it is advisable to make the following change of variables,

$$\hat{\phi}(\tau,\rho,x)=\hat{\phi}_{\log}(\tau,\rho,x)+\phi^c(\tau,\rho,x), \tag{A57}$$

$$\hat{\Sigma}(\tau,\rho,x)=\hat{\Sigma}_{\log}(\tau,\rho,x)+\Sigma^c(\tau,\rho,x), \tag{A58}$$

$$\hat{A}(\tau,\rho,x)=\hat{A}_{\log}(\tau,\rho,x)+A^c(\tau,\rho,x), \tag{A59}$$

$$\hat{\Xi}(\tau,\rho,x)=\hat{\Xi}_{\log}(\tau,\rho,x)+\Xi^c(\tau,\rho,x), \tag{A60}$$

and follow these numerical algorithms that we label with roman numerals below:

(i) At $\tau=\tau_i$, we have to start with an initial profile for the fields; our choice is

$$\begin{aligned}\phi^0_{l,n}&\equiv\phi^c(\tau_i,\rho_l,x_n),\\ \Sigma^0_{bl,n}&\equiv\Sigma^c_b(\tau_i,\rho_l,x_n),\end{aligned} \tag{A61}$$

with $\phi^0_{l,n}=\Sigma^0_{bl,n}=0$. These two initial profiles at τ_i are sufficient to solve Eq. (A39) and Eq. (A38) for all points on the lattice at time τ_i. For Σ_d, with definitions from Eq. (A57) and Eq. (A58) and inserting them into Eq. (A39), we can see that

$$\partial^2_\rho\Sigma^c_d=\tilde{J}_{\Sigma_d}, \tag{A62}$$

with

$$\begin{aligned}\tilde{J}_{\Sigma_d}=\partial^2_\rho\Sigma^d_{\log}+2\partial^2_\rho\Sigma^c_b+2\partial^2_\rho\Sigma^b_{\log}\\ +\frac{1}{2}(\partial_\rho\phi_c+\partial_\rho\phi_{\log})^2.\end{aligned} \tag{A63}$$

Then, in the above, we will use the initial profiles of $\phi^0_{l,n}$ and $\Sigma^0_{bl,n}$ to replace the ϕ_c and $\Sigma^b_{\log}$ and solve the above equation for the solution of $\Sigma^c_d(t_0,\rho,x)$, with the boundary conditions

$$\Sigma^{\rm con}(\tau,0,x)=0,\partial_\rho\Sigma^{\rm con}(\tau,0,x)=0 \tag{A64}$$

that have been derived from Eq. (A19). The matrix form of the differential equation is

$$(I_x\otimes D^2_\rho)\Sigma_{dl,n}=(\tilde{J}_{\Sigma_d})_{n,l}, \tag{A65}$$

where we impose the boundary conditions in a matrix form since $\Sigma_{dl,n}$ has a form similar to Eq. (A32). As is clear in Eq. (A63), in addition to the finite contributions of the fields Σ^c_b and ϕ_c on the right-hand side, we also need their logarithmic corrections. To subtract the logarithms, we make an expansion over the bulk radius. From Eq. (A17)–Eq. (A20), we have

$$\phi_{\log}=\log\rho\sum_{i=3}^{8}\frac{\rho^i}{(1+\rho)^{1+i}}\mathcal{F}_i[p_0(\tau,x)], \tag{A66}$$

$$\begin{aligned}\Sigma^{\log}_b&=\rho^2\log\rho\sum_{i=2}^{5}\frac{\rho^i}{(1+\rho)^{1+i}}\mathcal{B}_{1,i}[p_0(\tau,x),p_2(\tau,x)]\\ &\quad+\rho^2(\log\rho)^2\sum_{i=4}^{5}\frac{\rho^i}{(1+\rho)^{1+i}}\mathcal{B}_{2,i}[p_0(\tau,x)],\end{aligned} \tag{A67}$$

$$\begin{aligned}\Sigma^{\log}_d&=\rho^2\log\rho\sum_{i=2}^{7}\frac{\rho^i}{(1+\rho)^{1+i}}\mathcal{D}_{1,i}[p_0(\tau,x),p_2(\tau,x)]\\ &\quad+\rho^2(\log\rho)^2\sum_{i=4}^{7}\frac{\rho^i}{(1+\rho)^{1+i}}\mathcal{D}_{2,i}[p_0(\tau,x)],\end{aligned} \tag{A68}$$

with the coefficients of $\mathcal{F}_i$, $\mathcal{B}_{1,i}$, $\mathcal{B}_{2,i}$, $\mathcal{D}_{1,i}$ and $\mathcal{D}_{2,i}$ having a form that is rather complicated to mention here. As has been mentioned in Ref. [20], the upper bound for the series can go to infinity, but as is apparent from the first terms of Eq. (A67) and Eq. (A68), they are functions of p_2, an expansion parameter in the scalar field ϕ from Eq. (A17) (the normalizable mode). Since we have no information about this coefficient prior to solving the evolution equation for the scalar field, instead we use

$$p_2(\tau,x)=\frac{1}{6}\partial^3_\rho\phi(\tau,\rho,x)\big|_{\rho=1}. \tag{A69}$$

But the error in subtracting the coefficient in $p_2(\tau,x)$ stops us from increasing the upper bounds in Eq. (A67) and Eq. (A68).

(ii) Since we need time derivatives of $p_2(\tau,x)$ for evaluating the coefficients in Eq. (A67)–Eq. (A68), a time evolution of $\phi(\tau_i+\Delta\tau,\rho,x)$ is necessary. To do this, first, we solve Eq. (A38),

$$\left(I_x \otimes D_\rho - \frac{3}{2\rho}\right)\pi^{\tau_i}_{n,l} = -(J_\phi)_{n,l}, \tag{A70}$$

at τ_i with the boundary condition that reads

$$\pi^c(\tau_i, 0, x) = -\frac{p_0(\tau_i, x)}{2}. \tag{A71}$$

Then, in order to translate it to ϕ_c, we use

$$\begin{aligned}\partial_\tau \phi^c(\tau, \rho, x) = \pi^c(\tau_i, \rho, x) + \frac{1-\rho^4}{2}\partial_\rho \phi^c(\tau_i, \rho, x)\\ + k_{\log}(\tau_i, \rho, x),\end{aligned} \tag{A72}$$

with

$$\begin{aligned}k_{\log}(\tau_i, \rho, x) = \pi_{\log}(\tau_i, \rho, x) + \frac{1-\rho^4}{2}\partial_\rho \phi_{\log}(\tau_i, \rho, x)\\ - \partial_{\tau_i}\phi_{\log}(\tau_i, \rho, x).\end{aligned} \tag{A73}$$

The initial condition to solve Eq. (A72) is $\phi_c(-\infty, \rho, x) = 0$. Note that the forms of $\phi_{\log}$ and $\pi_{\log}$ are related according to Eq. (A57) and Eq. (A34). The latter is explicitly given by

$$\pi_{\log} = \log\rho \sum_{i=2}^{7} \frac{\rho^i}{(1+\rho)^i}\mathcal{P}_i[p_0(\tau, x)]. \tag{A74}$$

The evaluation is done by completing the first Runge-Kutta (RK) step,

$$k_{1,\phi} = \Delta\tau\left(\pi^{\tau_i}_{n,l} + \frac{1}{2}(1-\rho^4)\partial_\rho\phi^{\tau_i}_{n,l} + k_{\log}\right), \tag{A75}$$

that is accompanied by the following shifts,

$$\tau_i \to \tau_i + \frac{1}{2}\Delta\tau, \qquad \phi^{\tau_i}_{n,l} \to \phi^{\tau_i}_{n,l} + \frac{k_{1,\phi}}{2}, \tag{A76}$$

and with these new values for τ_i and $\phi^{\tau_i}_{n,l}$, we repeat RK step 1 to find $k_{2,\phi}$. This completes RK step 2. In RK step 3, we have

$$\tau_i \to \tau_i + \frac{1}{2}\Delta\tau, \qquad \phi^{\tau_i}_{n,l} \to \phi^{\tau_i}_{n,l} + \frac{k_{2,\phi}}{2}, \tag{A77}$$

and we repeat steps in RK step 1 to find $k_{3,\phi}$. At RK step 4, finally, we make the last set of shifts,

$$\tau_i \to \tau_i + \Delta\tau, \qquad \phi^{\tau_i}_{n,l} \to \phi^{\tau_i}_{n,l} + k_{3,\phi}, \tag{A78}$$

to obtain the value of the scalar field at $\tau = \tau_i + \Delta\tau$,

$$\phi^{\tau+\Delta\tau}_{n,l} = \phi^{\tau}_{n,l} + \frac{1}{6}k_{1,\phi} + \frac{1}{3}k_{2,\phi} + \frac{1}{6}k_{4,\phi}. \tag{A79}$$

This finishes the procedure of evaluating time derivatives of p_2 based on Eq. (A69). Knowing all the variables in Eq. (A62) allows us to evaluate $\Sigma^{\tau_i}_{dn,l} \equiv \Sigma_d(\tau_i, \rho, x)$.

(iii) In order to find $A^{\tau_i} \equiv A(\tau_i, \rho, x)$, we still need to evaluate the value of $\Xi^{\tau_i}_{n,l} \equiv \Xi(\tau_i, \rho, x)$. The values of $\phi^{\tau_i}_{n,l}$ and $\Sigma^{\tau_i}_{bn,l}$ are enough to do this as we describe in this section. Eq. (A40) on the lattice will be given by

$$\left(I_x \otimes D_\rho^2 - \frac{4}{\rho^2} + \frac{I_x \otimes D_\rho}{\rho}\right)\Xi^{\tau_i}_{n,l} = -(J_{\phi^{\tau_i}, \Sigma_b^{\tau_i}})_{n,l}, \tag{A80}$$

where the current $J_{\phi^{\tau_i}, \Sigma_b^{\tau_i}}$ are all the terms that include ϕ^{τ_i} and $\Sigma_b^{\tau_i}$ and have been taken to the right-hand side in Eq. (A40). We also need the logarithmic part $\Xi^{\log}$ subtracted by

$$\begin{aligned}\Xi^{\log} = \log\rho \sum_{i=2}^{5} \frac{\rho^i}{(1+\rho)^{1+i}}\mathcal{K}_{1,i}[p_0(\tau, x), p_2(\tau, x)]\\ + (\log\rho)^2 \frac{\rho^5}{(1+\rho)^6}\mathcal{K}_{2,5}[p_0(\tau, x)].\end{aligned} \tag{A81}$$

Once again, the boundary condition at $\rho = 0$ for solving Eq. (A80) is given by

$$\begin{aligned}\Xi^{\mathrm{con}}_f(\tau, 0, x) = 0,\\ \partial_\rho \Xi^{\mathrm{con}}_f(\tau, 0, x) = -\frac{1}{9}p_0\partial_x p_0.\end{aligned} \tag{A82}$$

(iv) As we mentioned before, knowing all the values of the fields $\phi^{\tau_i}_{n,l}$, $\Sigma^{\tau_i}_{bn,l}$ and $\Xi^{\tau_i}_{n,l}$, we can evaluate A^{τ_i} in principle from Eq. (A43) that has been deduced. Since it is a second-order differential equation with the two initial conditions that each will increase the size of the arrays (cost of the computation) by a factor of $N_x \times N_\rho$, we will rather replace for β and γ from Eq. (A41) and Eq. (A42) similarly to the approach of Ref. [20] in favor of a more complicated but linear equation for

$$\partial_\rho \tilde{A} = -J_{\tilde{A}}, \tag{A83}$$

with

$$\tilde{A} \equiv \partial_\rho^2 A + \frac{2}{\rho}\partial_\rho A, \tag{A84}$$

$$J_{\tilde{A}} \equiv \partial_\rho J_a + \frac{1}{\rho^2}\partial_\rho[\acute{J}_{\Sigma_d} + 2\acute{J}_{\Sigma_b}], \tag{A85}$$

and in the above, $\acute{J}$ refers to terms that are proportional to A in Js and have been taken to the left-hand side of Eq. (A83). Our boundary condition that is consistent with Eq. (A18) reads

$$\tilde{A}(t,0,x) = 6a_2 + \frac{5}{18}[(\partial_x p_0)^2 + 3(\partial_\tau p_0)^2 + p_0(\partial_x^2 p_0 - 3\partial_\tau^2 p_0)], \tag{A86}$$

where all the coefficients, p_0 and a_2, are functions of (τ, x). It is possible to rewrite Eq. (A83) in a more illuminating form,

$$\partial_\rho \tilde{A}_c = -\partial_\rho \tilde{A}_{\log} - J_{\tilde{A}}, \tag{A87}$$

with

$$\tilde{A}_c = \partial_\rho^2 A_c + \frac{2}{\rho}\partial_\rho A_c,$$
$$\tilde{A}_{\log} = \partial_\rho^2 A_{\log} + \frac{2}{\rho}\partial_\rho A_{\log}, \tag{A88}$$

and $J_{\tilde{A}}$ given in Eq. (A85) with $A_{\log}$, having the form

$$A^{\log} = \log\rho \sum_{i=2}^{5} \frac{\rho^i}{(1+\rho)^{1+i}} \mathcal{A}_{1,i}[p_0(\tau,x), p_2(\tau,x)] + (\log\rho)^2 \sum_{i=4}^{5} \frac{\rho^i}{(1+\rho)^{1+i}} \mathcal{A}_{2,i}[p_0(\tau,x)]. \tag{A89}$$

The differential equation in Eq. (A87) will accordingly take the simple matrix form

$$(I_x \otimes D_\rho)\tilde{A}^{\tau_i}_{n,l} = -(J_{\tilde{A}^{\tau_i}})_{n,l} - (\partial_\rho \tilde{A}^{\tau_i})_{n,l}, \tag{A90}$$

and it is an easy exercise to implement the boundary condition Eq. (A86). Note that the boundary condition of $\tilde{A}^{\tau_i}_{n,l}$ in Eq. (A86) depends on the coefficient a_2 defined in Eq. (A18). This means that in order to solve the set of the above equations, we need to provide an initial profile,

$$(a_2^{\tau_i})_{n,l} \equiv a_2(\tau_i, \rho, x). \tag{A91}$$

Our choice is $(a_2^{\tau_i})_{n,l} = 0$. Finally, we will transform the value obtained from $\tilde{A}^{\tau_i}_{n,l}$ to $A^{\tau_i}_{n,l}$ according to Eq. (A84) by integration.

(v) At this point, we have access to the value of the scalar field and all the components of the metric in the whole plane of the lattice but only at the initial time τ_i. The goal is to extend our computation to later times. This being said, on the other hand, we started the computation at the beginning of our numerical algorithm by introducing the initial profile for $(\Sigma_b^{\tau_i})_{n,l}$ by hand. Clearly, this initial profile at different times must evolve, too. This brings us to the coupled equations of Eq. (A41)–Eq. (A42),

$$\partial_\rho \beta - \frac{1}{\rho}[2\beta + \gamma] = -J_{\Sigma_d}, \tag{A92}$$

$$\partial_\rho \gamma - \frac{1}{2\rho}[\beta + 5\gamma] = -J_{\Sigma_b}, \tag{A93}$$

with the corresponding assignments in Eq. (A35) and Eq. (A36),

$$\beta(\tau,\rho,x) = \partial_\tau \hat{\Sigma}_d(\tau,\rho,x) + \frac{\rho^4 - 1}{2}\partial_\rho \hat{\Sigma}_d(\tau,\rho,x), \tag{A94}$$

$$\gamma(\tau,\rho,x) = \partial_\tau \hat{\Sigma}_b(\tau,\rho,x) + \frac{\rho^4 - 1}{2}\partial_\rho \hat{\Sigma}_b(\tau,\rho,x), \tag{A95}$$

and the sources J_{Σ_d} and J_{Σ_b} that are defined in Eq. (A46) and Eq. (A47). Since they are functions of the known fields at τ_i, we can solve the coupled differential equations with the following boundary conditions:

$$\beta^c(\tau,0,x) = \gamma^c(\tau,0,x) = 0. \tag{A96}$$

Since on the lattice we deal with finite variables occasionally, we will be sloppy about mentioning the subindex c for the scalar field and various metric components.

Upon splitting the finite and logarithmic corrections in Eq. (A92) and Eq. (A93), they take the form

$$\partial_\rho \beta_c - \frac{1}{\rho}(\gamma_c + 2\beta_c) = -J_{\Sigma_d} - \partial_\rho \beta_{\log} + \frac{1}{\rho}(2\beta_{\log} + \gamma_{\log}), \tag{A97}$$

$$\partial_\rho \gamma_c - \frac{1}{2\rho}(\beta_c + 5\gamma_c) = -J_{\Sigma_b} - \partial_\rho \gamma_{\log} + \frac{1}{2\rho}(\beta_{\log} + 5\gamma_{\log}), \tag{A98}$$

where the logarithmic corrections to β and γ are calculated from Eq. (A35),

$$\beta^{\log} = \log\rho \sum_{i=3}^{6} \frac{\rho^i}{(1+\rho)^i} \tilde{\mathcal{D}}_{1,i}[p_0(\tau,x), p_2(\tau,x)] + (\log\rho)^2 \sum_{i=5}^{6} \frac{\rho^i}{(1+\rho)^i} \tilde{\mathcal{D}}_{2,i}[p_0(\tau,x)], \tag{A99}$$

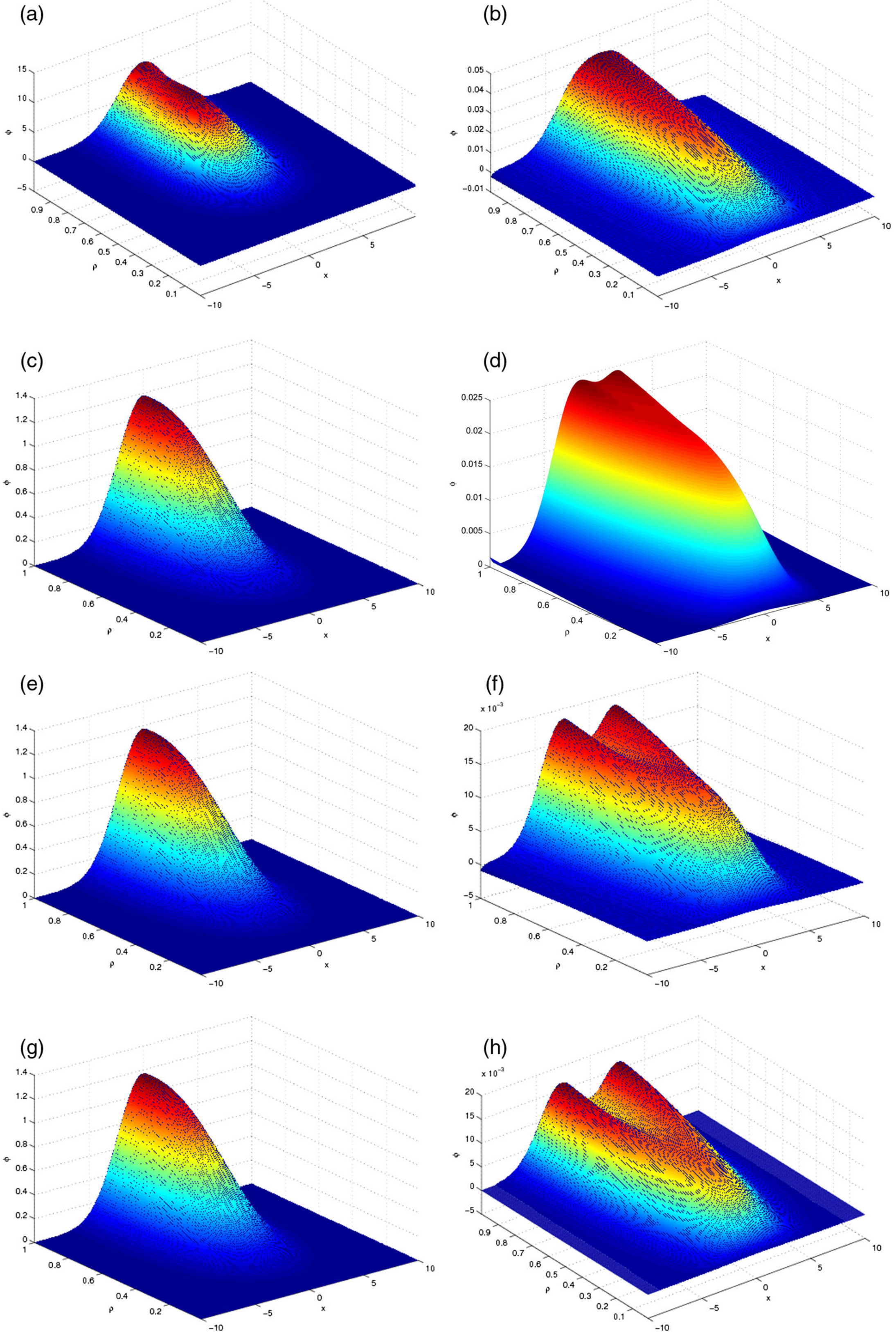

FIG. 11. Plots of $\phi(\tau, \rho, x)$ at two specific times. On the left-hand sides, the quench has not been switched on. Specifically, these plots show the configuration at $\tau = -3.75$. At some time long after the quench, for instance, $\tau = 12$, the profiles for $\phi(\tau, \rho, x)$ are shown on the right-hand sides. Dimensions of lattices from the first to the last row are respectively given by 20×20, 30×30, 40×40 and 50×50. Fixed parameters are $\alpha = 1$ and $\sigma = \sqrt{L_x}$.

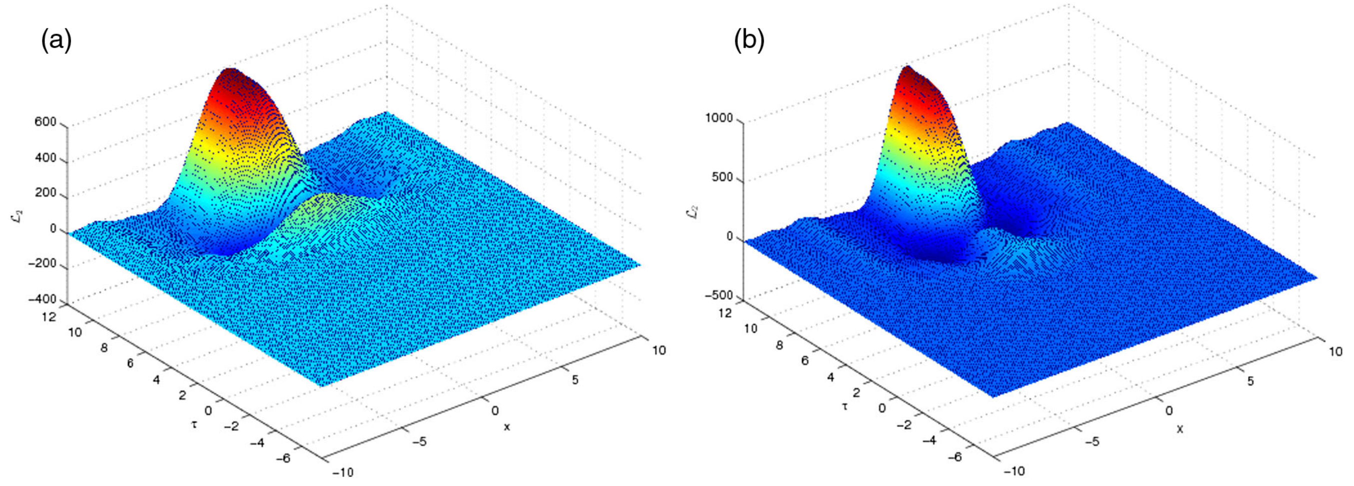

FIG. 12. The effect of the numerical instabilities coming from the RK method shown for the two-point function. Here, in both diagrams, $N_x = N_\rho = 20$. The time step for the left-hand diagram is $\Delta\tau$ and half of this value for the plot on the right-hand side.

$$\gamma^{\log} = \log\rho \sum_{i=3}^{6} \frac{\rho^i}{(1+\rho)^i} \tilde{\mathcal{B}}_{1,i}[p_0(\tau,x), p_2(\tau,x)] + (\log\rho)^2 \sum_{i=5}^{6} \frac{\rho^i}{(1+\rho)^i} \tilde{\mathcal{B}}_{2,i}[p_0(\tau,x)]. \tag{A100}$$

In the matrix form, we can rewrite Eq. (A92)–Eq. (A93), in the following way,

$$\begin{pmatrix} I_x \otimes D_\rho & -\frac{1}{\rho} \\ -\frac{1}{2\rho} & I_x \otimes D_\rho - \frac{5}{2\rho} \end{pmatrix} \begin{pmatrix} \beta^{\tau_i} \\ \gamma^{\tau_i} \end{pmatrix}_{n,l} = - \begin{pmatrix} \tilde{J}_{\Sigma_d^{\tau_i}} \\ \tilde{J}_{\Sigma_b^{\tau_i}} \end{pmatrix}_{n,l}, \tag{A101}$$

with $\tilde{J}_{\Sigma_d^{\tau_i}}$ and $\tilde{J}_{\Sigma_b^{\tau_i}}$ that include terms such as $\beta_{\log}$, $\gamma_{\log}$ and their derivative as they appear on the right-hand side of Eq. (A97) and Eq. (A98). This yields $\beta^{\tau_i}_{n,l}$ and $\gamma^{\tau_i}_{n,l}$ at the initial time $\tau = \tau_i$. Now, similarly to the procedure mentioned in detail for the scalar field $\phi^{\tau_i}_{n,l}$, we can perform four steps of the RK method to evaluate Eq. (A94)–Eq. (A95) for $\tau = \tau_i + \Delta\tau$. This is the last stage of our simulation, and all the steps that we have done so far will be repetitively performed until the desired final time $\tau = \tau_f$ is reached.

Discretization.—In this section, we look at the effect of the discretization and possible sources of numerical artifacts. There are two main sources of numerical artifacts: the chosen number of points on the lattice and the chosen value for the time steps $\Delta\tau$. One advantage of having an observable as a function of two coordinates is that numerical instabilities or artifacts, if any, are hard to miss. Therefore, the best method is just to change the number of lattice points and compare them.

For simplicity, all of the lattices that we have considered are square lattices with $N_x = N_\rho$. As an example, we compared $\phi(\tau,\rho,x)$ for lattices with 20×20, 30×30, 40×40 and 50×50 at two specific times, early before ($\tau = -3.75$) and a long time after turning on the quench ($\tau = 12$). The corresponding plots are shown in Fig. 11.

The other source of numerical instability is the value chosen for the marching steps in the Runge-Kutta method. Below, we compare one of the observables computed in the paper, $\mathcal{L}_2$, the two-point function for case I, for two different time steps, $\Delta\tau$ and $\frac{\Delta\tau}{2}$.

Numerical instabilities that are produced this way are specifically dominant for a region near $\rho \sim 1$. Observables in our computation, such as entanglement entropies that depend on Taylor expansions of the metric near $\rho \sim 0$, are the least affected quantities by these instabilities. This is mainly due to the fact that we have calculated their expansions up to $\mathcal{O}(\rho^8)$ analytically using the Einstein equations. This in part allows us to use a lower number of lattice points for simulating them.

This check is the most time-consuming part. For a lattice of $N_x = N_\rho = 20$ points, this takes roughly a month. For a lattice of $N_x = N_\rho = 30$, this process takes two months. Different observables for various parameters have been executed on different nodes. It takes three days to produce a single plot for a parallelized code on a 16-core node. The corresponding plots are shown in Fig. 12.

b. Thermalization.—In the same category, we look at the effects of the lattice artifacts on the thermalization. The normalizable mode in the expansion of the bulk scalar allows us to observe this since this is the response to the mass gap. Practically, the numerical algorithm was designed to stop when the standard deviation from the mean value goes below 10^{-11} while in the trend toward thermalization. We plot the dynamical evolution of this component of the scalar field for various lattice sizes in Fig. 13. The standard deviations from the mean values at late times are given in the table below:

Measure of thermalization N_x or N_ρ	N_τ	Standard deviation
20	7810	8.9×10^{-12}
30	17560	3.5×10^{-13}
40	31210	1.7×10^{-13}
50	41272	2.1×10^{-13}

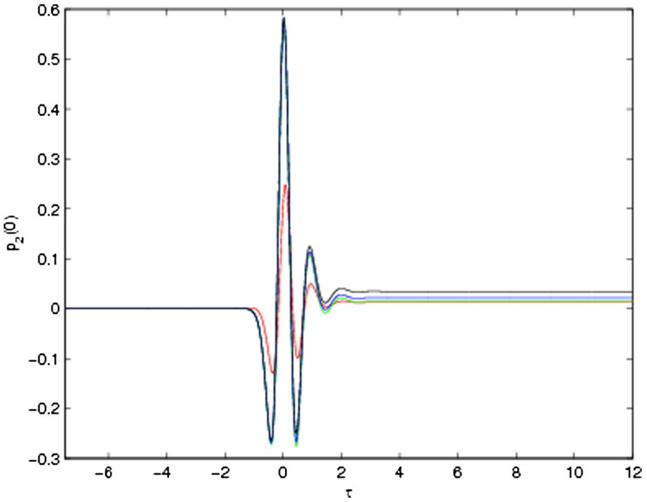

FIG. 13. Evolution of the normalizable mode of the scalar field on various lattice sizes. Black color for $N_x = N_\rho = 20$, blue for $N_x = N_\rho = 30$, green for $N_x = N_\rho = 40$ and red for $N_x = N_\rho = 50$.

[1] K. Adcox *et al.* (PHENIX Collaboration), Formation of dense partonic matter in relativistic nucleus nucleus collisions at RHIC: Experimental evaluation by the PHENIX collaboration, Nucl. Phys. **A757**, 184 (2005); B. B. Back *et al.* (PHOBOS Collaboration), The PHOBOS perspective on discoveries at RHIC, Nucl. Phys. **A757**, 28 (2005); I. Arsene *et al.* (BRAHMS Collaboration), Quark gluon plasma and color glass condensate at RHIC? The perspective from the BRAHMS experiment, Nucl. Phys. **A757**, 1 (2005); J. Adams *et al.* (STAR Collaboration), Experimental and theoretical challenges in the search for the quark gluon plasma: The STAR collaboration's critical assessment of the evidence from RHIC collisions, Nucl. Phys. **A757**, 102 (2005).

[2] D. Teaney, J. Lauret, and E. V. Shuryak, Flow at the SPS and RHIC as a Quark Gluon Plasma Signature, Phys. Rev. Lett. **86**, 4783 (2001); P. Huovinen, P. F. Kolb, U. W. Heinz, P. V. Ruuskanen, and S. A. Voloshin, Radial and elliptic flow at RHIC: Further predictions, Phys. Lett. B **503**, 58 (2001); P. F. Kolb, U. W. Heinz, P. Huovinen, K. J. Eskola, and K. Tuominen, Centrality dependence of multiplicity, transverse energy, and elliptic flow from hydrodynamics, Nucl. Phys. **A696**, 197 (2001); T. Hirano and K. Tsuda, Collective flow and two pion correlations from a relativistic hydrodynamic model with early chemical freeze out, Phys. Rev. C **66**, 054905 (2002); P. F. Kolb and R. Rapp, Transverse flow and hadro-chemistry in Au+Au collisions at s(NN) (1/2)= 200-GeV, Phys. Rev. C **67**, 044903 (2003).

[3] P. B. Arnold, G. D. Moore, and L. G. Yaffe, Transport coefficients in high temperature gauge theories. 1. Leading log results, J. High Energy Phys. 11 (2000) 001; Photon emission from ultrarelativistic plasmas, J. High Energy Phys. 11 (2001) 057; Photon emission from quark gluon plasma: Complete leading order results, J. High Energy Phys. 12 (2001) 009; Transport coefficients in high temperature gauge theories. 2. Beyond leading log, J. High Energy Phys. 05 (2003) 051.

[4] J. M. Maldacena, The large N limit of superconformal field theories and supergravity, Int. J. Theor. Phys. **38**, 1113 (1999); Adv. Theor. Math. Phys. **2**, 231 (1998); O. Aharony, S. S. Gubser, J. M. Maldacena, H. Ooguri, and Y. Oz, Large N field theories, string theory and gravity, Phys. Rep. **323**, 183 (2000).

[5] P. M. Chesler and L. G. Yaffe, Horizon Formation and Far-from-Equilibrium Isotropization in Supersymmetric Yang-Mills Plasma, Phys. Rev. Lett. **102**, 211601 (2009).

[6] M. P. Heller, D. Mateos, W. van der Schee, and D. Trancanelli, Strong Coupling Isotropization of Non-Abelian Plasmas Simplified, Phys. Rev. Lett. **108**, 191601 (2012); P. M. Chesler and L. G. Yaffe, Holography and Colliding Gravitational Shock Waves in Asymptotically AdS_5 Spacetime, Phys. Rev. Lett. **106**, 021601 (2011); F. Carrasco, L. Lehner, R. C. Myers, O. Reula, and A. Singh, Turbulent flows for relativistic conformal fluids in $2+1$ dimensions, Phys. Rev. D **86**, 126006 (2012); M. P. Heller, R. A. Janik, and P. Witaszczyk, A numerical relativity approach to the initial value problem in asymptotically Anti-de Sitter spacetime for plasma thermalization—An ADM formulation, Phys. Rev. D **85**, 126002 (2012); L. Lehner, Numerical relativity: A Review, Classical Quantum Gravity **18**, R25 (2001).

[7] P. Calabrese and J. L. Cardy, Evolution of entanglement entropy in one-dimensional systems, J. Stat. Mech. 0504, P04010 (2005).

[8] S. Sotiriadis and J. Cardy, Inhomogeneous quantum quenches, J. Stat. Mech. 11, P11003 (2008).

[9] P. Calabrese and J. L. Cardy, Time-Dependence of Correlation Functions Following a Quantum Quench, Phys. Rev. Lett. **96**, 136801 (2006); P. Calabrese and J. Cardy, Quantum quenches in extended systems, J. Stat. Mech. 0706, P06008 (2007); P. Calabrese, C. Hagendorf, and P. Le Doussal, Time evolution of 1D gapless models from a domain-wall initial state: SLE continued? J. Stat. Mech. 2008, P07013 (2008); C. Kollath, A. Laeuchli, and E. Altman, Quench Dynamics and Nonequilibrium Phase Diagram of the Bose-Hubbard Model, Phys. Rev. Lett. **98**, 080601 (2006); M. Cramer, C. M. Dawson, J. Eisert, and T. J. Osborne, Exact Relaxation in a Class of Non-Equilibrium Quantum Lattice Systems, Phys. Rev. Lett. **100**, 030602 (2008); G. Roux, Quenches in quantum many-body systems: One-dimensional Bose-Hubbard model reexamined, Phys. Rev. A **79**, 021608 (2009); S. Sotiriadis, P. Calabrese, and J. Cardy, Quantum quench from a thermal initial state, Europhys. Lett. **87**, 20002 (2009); M. Rigol, V. Dunjko, V. Yurovsky, and M. Olshanii, Relaxation in a Completely Integrable Many-Body Quantum System: An *Ab Initio* Study of the Dynamics of the Highly Excited States of Lattice Hard-Core Bosons, Phys. Rev. Lett. **98**, 4 (2006); S. R. Manmana, S. Wessel, R. M. Noack, and A. Muramatsu, Strongly Correlated Fermions after a Quantum Quench, Phys. Rev. Lett. **98**, 4 (2006); P. Calabrese, F. H. L. Essler, and M. Fagotti, Quantum Quench in the Transverse Field Ising Chain, Phys. Rev. Lett. **106**, 227203 (2011); S. Sotiriadis and J. Cardy, Quantum quench in interacting field theory: A Self-consistent approximation, Phys. Rev. B **81**, 134305 (2010); S. R. Das and K. Sengupta, Non-equilibrium dynamics of O(N) nonlinear sigma models: A large-N approach, J. High Energy Phys. 09 (2012) 072; L.-Y. Hung, M. Smolkin, and E. Sorkin, Modification of Late Time Phase Structure by Quantum Quenches, Phys. Rev. Lett. **109**, 155702 (2012); Modification of late time phase structure by quantum quenches, J. High Energy Phys. 09 (2012) 072; E. Caceres, A. Kundu, J. F. Pedraza, and D. L. Yang, Weak field collapse in AdS: Introducing a charge density, J. High Energy Phys. 06 (2015) 111.

[10] R. Donagi and E. Witten, Supersymmetric Yang-Mills theory and integrable systems, Nucl. Phys. **B460**, 299 (1996).

[11] K. Pilch and N. P. Warner, $N = 2$ supersymmetric RG flows and the IIB dilaton, Nucl. Phys. **B594**, 209 (2001).

[12] A. Buchel, S. Deakin, P. Kerner, and J. T. Liu, Thermodynamics of the N=2* strongly coupled plasma, Nucl. Phys. **B784**, 72 (2007).

[13] A. Khavaev, K. Pilch, and N. P. Warner, New vacua of gauged $N = 8$ supergravity in five-dimensions, Phys. Lett. B **487**, 14 (2000).

[14] N. J. Evans, C. V. Johnson, and M. Petrini, The enhancon and $N = 2$ gauge theory: Gravity RG flows, J. High Energy Phys. 10 (2000) 022.

[15] C. Hoyos, S. Paik, and L. G. Yaffe, Screening in strongly coupled N=2* supersymmetric Yang-Mills plasma, J. High Energy Phys. 10 (2011) 062.

[16] A. Buchel and J. T. Liu, Thermodynamics of the N=2* flow, J. High Energy Phys. 11 (2003) 031.

[17] A. Buchel, N=2* hydrodynamics, Nucl. Phys. **B708**, 451 (2005).

[18] S. Kobayashi, D. Mateos, S. Matsuura, R. C. Myers, and R. M. Thomson, Holographic phase transitions at finite baryon density, J. High Energy Phys. 02 (2007) 016.

[19] A. Buchel, L. Lehner, and R. C. Myers, Thermal quenches in N=2* plasmas, J. High Energy Phys. 08 (2012) 049.

[20] A. Buchel, R. C. Myers, and A. van Niekerk, Nonlocal probes of thermalization in holographic quenches with spectral methods, J. High Energy Phys. 02 (2015) 017.

[21] M. Rigol, V. Dunjko, and M. Olshanii, Thermalization and its mechanism for generic isolated quantum systems, Nature (London) **452**, 854 (2008).

[22] P. M. Chesler and L. G. Yaffe, Numerical solution of gravitational dynamics in asymptotically anti-de Sitter spacetimes, J. High Energy Phys. 07 (2014) 086.

[23] A. Buchel, L. Lehner, R. C. Myers, and A. van Niekerk, Quantum quenches of holographic plasmas, J. High Energy Phys. 05 (2013) 067.

[24] R. Auzzi, S. Elitzur, S. B. Gudnason, and E. Rabinovici, On periodically driven AdS/CFT, J. High Energy Phys. 11 (2013) 016.

[25] A. Buchel, R. C. Myers, and A. van Niekerk, Universality of Abrupt Holographic Quenches, Phys. Rev. Lett. **111**, 201602 (2013).

[26] S. R. Das, D. A. Galante, and R. C. Myers, Universal scaling in fast quantum quenches in conformal field theories, Phys. Rev. Lett. **112**, 171601 (2014); Universality in fast quantum quenches, J. High Energy Phys. 02 (2015) 167.

[27] V. Balasubramanian and S. F. Ross, Holographic particle detection, Phys. Rev. D **61**, 044007 (2000); J. Louko, D. Marolf, and S. F. Ross, On geodesic propagators and black hole holography, Phys. Rev. D **62**, 044041 (2000).

[28] G. Aarts and J. Smit, Particle production and effective thermalization in inhomogeneous mean field theory, Phys. Rev. D **61**, 025002 (1999).

[29] S. Ryu and T. Takayanagi, Holographic Derivation of Entanglement Entropy from AdS/CFT, Phys. Rev. Lett. **96**, 181602 (2006); Aspects of holographic entanglement entropy, J. High Energy Phys. 08 (2006) 045.

[30] J. Abajo-Arrastia, J. Aparicio, and E. Lopez, Holographic evolution of entanglement entropy, J. High Energy Phys. 11 (2010) 149; H. Liu and S. J. Suh, Entanglement growth during thermalization in holographic systems, Phys. Rev. D **89**, 066012 (2014); L. Y. Hung, R. C. Myers, and M. Smolkin, Some calculable contributions to holographic entanglement entropy, J. High Energy Phys. 08 (2011) 039; H. Liu and M. Mezei, A refinement of entanglement entropy and the number of degrees of freedom, J. High Energy Phys. 04 (2013) 162; R. C. Myers and A. Singh, Comments on holographic entanglement entropy and RG flows, J. High Energy Phys. 04 (2012) 122.

[31] V. Balasubramanian, A. Bernamonti, J. de Boer, B. Craps, L. Franti, F. Galli, E. Keski-Vakkuri, B. Müller, and A. Schäfer, Inhomogeneous Thermalization in Strongly Coupled Field Theories, Phys. Rev. Lett. **111**, 231602 (2013); V. Balasubramanian, A. Bernamonti, N. Copland, B. Craps, and F. Galli, Thermalization of mutual and tripartite information in strongly coupled two dimensional conformal field theories, Phys. Rev. D **84**, 105017 (2011).

[32] D. Giataganas, Probing strongly coupled anisotropic plasma, J. High Energy Phys. 07 (2012) 031.

[33] J. C. Mason and D. Hanscomb, *Chebyshev Polynomials* (Chapman and Hall/CRC Press, Florida, 2003).

[34] W. Guo, G. Labrosse, and R. Narayanan, *The Application of the Chebyshev-Spectral Method in Transport Phenomena*, Lecture Notes in Applied and Computational Mechanics (Springer-Verlag, Berlin, 2012), Vol. 68.